

RESEARCH ARTICLE

Mechanical changes and analysis of heat-treated 4140 steel with Taguchi method and ANOVA

Halil Ibrahim Kurt¹, Utku Berk Akyuz², Engin Ergul³¹Aerospace Engineering, Faculty of Aeronautics and Astronautics, University of Samsun, Türkiye²Department of Metallurgical and Materials Engineering, Engineering Faculty, Gaziantep University, Türkiye³Machinery and Metal Technologies Department, Izmir Vocational School, Dokuz Eylul University, Türkiye

Article Info

Article history:

Received: 21.11.2022

Revised: 17.12.2022

Accepted: 26.12.2022

Published Online: 04.03.2023

Keywords:

4140 steel
Heat treatment
Tempering
Taguchi
ANOVA

Abstract

In this work, the heat treatment process is applied to the 4140 steel to see how the samples show mechanical changes under various conditions. The samples have a height and diameter of 20 mm and 10 mm. The samples are heated up to 800 and 850 °C and then cooled in oil or oil and water mixture. The samples were annealed at 150 and 300 degrees for 1 and 3 h, respectively. After these stages, the microscope images of the samples are taken by optical and SEM microscopes. In addition to these, hardness tests are conducted on the specimens and results are analyzed by the Taguchi method with ANOVA. Because of these tests, the properties of the samples were fixed and discussed. The process variations affected the hardness values of the samples. The maximum hardness is obtained on the sample the hardened in the mixture of the oil and water. The DOE analysis confirmed the experimental results and showed the minimum error and maximum consistency.

1. Introduction

Steel is an alloy made up of the elements iron and carbon, which typically range in concentration from 0.02 to 2.1 percent [1–3]. The categorization of steel is actively influenced by how much carbon is present in the steel alloy. The steels mechanical and physical characteristics of change depend on how much carbon is contained in them. Steels are divided into three classes based on the proportion of carbon in each category; i) low carbon steels ii) medium carbon steels and iii) high carbon steel.

AISI 4140 steel is a medium carbon Cr–Mo steel used for applications requiring strength and impact toughness. It possesses great fatigue strength and wear resistance [4–8] as well as the ability to withstand temperatures up to 480°C, making it ideal for high-stress applications. In this article, the heat treatments are applied on the 4140 steel, we will see how the sample shows mechanical changes under what conditions and what differences it creates when heated to the same temperature and different cooling methods are used. Unalloyed and alloyed machine-building steels with a carbon content that are particularly suited for hardening, 4140 steels exhibit excellent toughness at a specific tensile strength at the conclusion of the curing process. 4140 steel, which has good induction qualities, may be summed up as an incredibly strong and high-quality material [9–11]. Due to a combination of these qualities, 4140 grade-tempered steel is currently a very sought-after product on the market. 4140 steel, which has good induction qualities, may be summed as an incredibly strong and high-quality material. Due to a combination of these qualities, 4140 grade-tempered steel is currently a very sought-after product on the market. These steels can be used individually as unalloyed, manganese alloyed, chromium, and chromium-molybdenum alloys based on their chemical compositions.

Since steels are used more in industries than other metals and alloys, heat treatment of steels has special importance [12].

Depending on the phase diagrams of metals and alloys, the desired mechanical properties and microstructures can be obtained with different processes applied at temperatures below the melting temperature. Heat treatment is mostly used to improve the metallic properties of metals. It comes to the forefront in terms of shape, especially with hardness and strength. It is also applied to make some changes in the properties of a metal part. 4140 tempered steel crankshaft, spline shaft, axle shaft and sleeve etc. used in various parts. Additionally, machinery parts and apparatus, agricultural vehicles and machinery, defense industry production, oil and gas industry are various usage areas of 4140 tempered steel [13], [14]. AISI 4140 steels must have a certain hardness value. Verma and Singh investigated the mechanical properties of AISI 1040 steel [15]. The authors noted that the highest hardness is obtained at the lowest temperature and the hardness reduced with increasing tempering temperature and holding time. Çaligulu et al. declared that the tempering temperature of the steels affects the martensitic transformation and the temperature decreases the hardness [16]. The media of the water and ash are compared and the highest hardness is obtained by water cooling [17]. The influence of double quenching and tempering with conventional quenching and tempering on the microstructure and mechanical properties of AISI 4140 steel was compared and it found that the specimens the double quenched and tempered indicated much higher mechanical properties than the specimens conventional quenched and tempered owing to finer austenite grain size, finer martensitic packets and a lower level of impurity concentration [18]. The low-cycle fatigue properties of AISI 4140 steel were significantly improved by the annealing treatment [19].

The study aims to investigate the influences of the homogenization and tempering temperatures and tempering time and the cooling rate on the hardness and microstructure of

AISI 4140 steel and compare the results with the Taguchi [20], [21] method with ANOVA [22,23].

2. Materials and methods

In this article, the heat treatments are applied on the 4140 steel, we will see how the sample shows mechanical changes under what conditions and what differences it creates when heated to the same temperature and different cooling methods are used. The composition of the samples is given in Table 1. The heat-treated samples are 30 mm long and 10 mm in diameter, as shown Fig. 1.

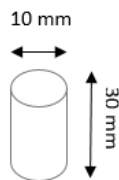


Figure 1. The schematic drawing of samples

As a heat treatment application, the samples are heated up to 800 and 850 °C and then cooled in oil and oil-water mixture (50 wt.% + 50 wt.%). Additionally, the samples were annealed at 150 and 300 degrees for 1 and 3 h at different temperatures and for different times. After these stages, the samples were sanded, polished and etched. For 50 seconds, the polished samples were etched in 96 ml HNO₃ – 4 ml HCl reagent. Then, the microstructures are studied with an optical microscope and SEM. The hardness test results were taken with ten reading averages and analyzed by the Taguchi method with ANOVA.

Table 1. Chemical composition of 4140 steel (wt%).

| C | Si | Mn | P | S | Cr | Mo | Fe |
|------|------|------|-------|-------|------|------|-----|
| 0.45 | 0.35 | 0.75 | 0.017 | 0.019 | 1.19 | 0.21 | Bal |

3. Results and discussion

In the Table 2, the experimental process and results are given. Heat-treated samples are in oil and the mixture of oil and water. The homogenous temperature, tempering temperature and time are changed and the hardness results are presented in Table 2. The samples displayed the different hardness values owing to various process parameters. The minimum and maximum hardness values of the heat-treated steels in oil are 153.57 HV and 568.77 HV, respectively, and 435.20 HV and

622.17 HV, respectively, for the heat-treated steels of the mixture of oil+water.

While the tempering temperature (150 °C) and tempering time (1 h) are constant for the oil hardened, the hardness increased when the homogenization temperature increased from 800 (°C) to 850 (°C). For the tempering temperature of 300 °C and tempering time of 3 h, the hardness decreased when the homogenization temperature increased from 800 (°C) to 850 (°C). In the mixture of oil and water, the hardness increased when the homogenization increased from 800 (°C) to 850 (°C) while the tempering temperature (150 °C) and tempering time (1 h) are constant. It is not seen an important change the hardness with the changing of the homogenization temperature from 800 (°C) to 850 (°C) for the tempering temperature of 300 °C and tempering time of 3 h. In oil quenching, the cooling rate in oil is slower than the cooling rate in water. As seen in this study, the reason for the obtained the higher hardness in the mixture of the oil and water compared to oil is the higher the cooling rate of the mixture of the oil and water [24–26].

In Fig. 2, a martensitic structure formed due to the cooling effect in the oil and mixture of the oil and water. The microstructures are taken and presented to the minimum and maximum hardness results. In the microstructures, the grain coarsening is observed in the microstructures with increasing temperature (Fig. 2a-b). The martensitic structure and plates in Fig. 2d form to a ferritic structure with the increasing of the tempering temperature and tempering time (Fig. 2a-b). For the mixture of oil and water hardened steels, the intense perlite structure is relocated with a ferritic structure, as seen in Fig. 2e-f. Before and after the tempering process, the temperature and time are carefully selected for temper embrittlement, which is generally seen in the temperature range of 400–600 °C [27].

Time-temperature-transformation (TTT) and continuous-cooling-transformation (CCT) diagrams are shown in Fig. 3. TTT diagrams are used to examine the multifaceted events that occur during the austenite transformation and primarily determine the properties of the transformation product. CCT diagrams show transformation events depending on temperature and time. With the help of the CCT diagram, the structures that will form in the steel are seen at the end of the preferred cooling rates. It can be very clearly seen that the structure will completely transform into martensite with very rapid cooling from the austenite phase temperature. The Ms temperature of 4140 steel is approximately 300–350 °C according to the continuous cooling transformation diagram.

Table 2. Experimental Process and Results

| Hardening Media | Homogenization Temperature (°C) | Tempering Temperature (°C) | Tempering Time (h) | Hardness (HV) | Code |
|---------------------------|---------------------------------|----------------------------|--------------------|---------------|------|
| Oil | 800 | 150 | 1 | 479.20 | A |
| | 800 | 300 | 3 | 235.20 | B |
| | 850 | 150 | 1 | 568.77 | C |
| | 850 | 300 | 3 | 153.57 | D |
| Oil wt.50% + Water wt.50% | 800 | 150 | 1 | 603.90 | E |
| | 800 | 300 | 3 | 436.67 | F |
| | 850 | 150 | 1 | 622.17 | G |
| | 850 | 300 | 3 | 435.20 | H |

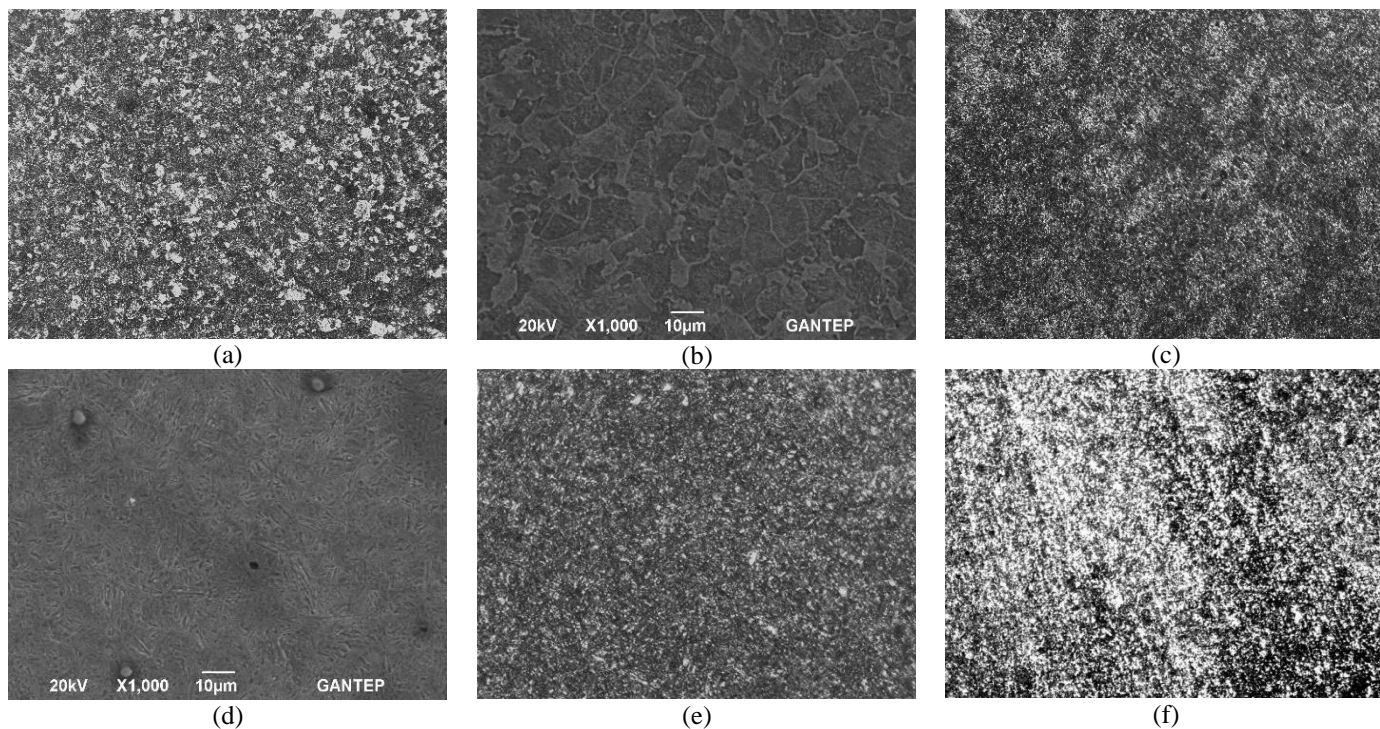


Figure 2. a) Optical and b) SEM images of sample D, c) Optical, and d) SEM images of sample B, Optical images of e) sample G and f) sample H

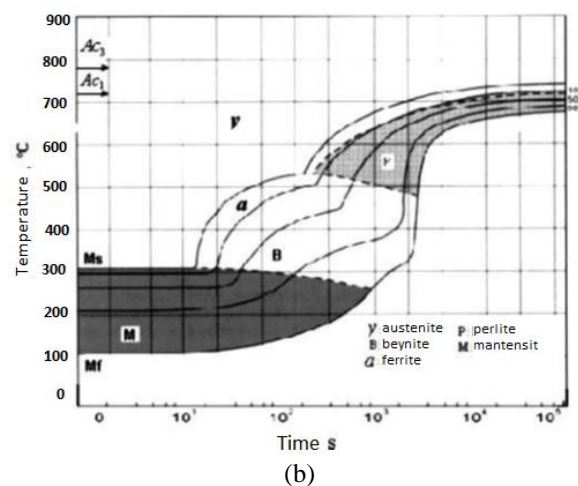
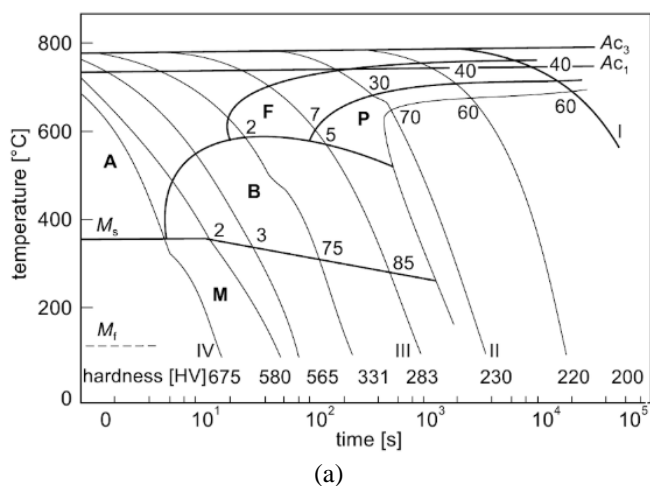


Figure 3. a) TTT and b) CTT diagrams of 4140 steel [28]

The authors declared that while the transformation from a martensitic structure to bainitic or ferritic structure is observed in steels depending on the tempering temperature, the hardness values also decrease depending on the tempering temperature [16]. Similar results are also reported in the related studies [29], [30]. The changes in the homogenization temperature, tempering temperature and tempering time affect the mechanical properties of the samples. Thus, a detail analysis of the results must be done. In this work, we studied the results with the experiment of design (DOE) with ANOVA for this aim.

4. Experiment of design (DOE)

The Taguchi method was used as the experimental design and analysis method. The main steps of this method are (1) determining the factors and interactions, (2) determining the levels of each factor, (3) choosing the appropriate orthogonal matrix, (4) transferring the factors and interactions to the columns of the orthogonal matrices, (5) performing the

experiments, (6) analysis of data and determining of optimal levels, and (7) performing validation experiments [31]. The parameters and levels given in Table 2 are used to determine some parameters and their levels effective in adsorption with the Taguchi technique. For this purpose, Taguchi experimental design with 2 parameters and three levels, L4 (2³) orthogonal array, is extracted using the Minitab program [32,33]. The characteristic of the system is its performance with Larger-the-Better using the Equal 1.

$$\frac{s}{N} = -10 \log_{10} \left(\frac{1}{n} \sum_{i=1}^n \frac{1}{y^2} \right) \tag{Eq. 1}$$

Where:

- y = Response value
- y' = Mean of the response value
- s = Standard deviation
- n = Number of trails in given experiment

Table 3. The statistical results for hardened steel in the oil

| Level | Homogenization Temperature (°C) | Tempering Temperature (°C) | Tempering Time (h) | Code | S/N ratio |
|-------|---------------------------------|----------------------------|--------------------|------|-----------|
| 1 | 50.52 | 54.35 | 48.67 | A | 53.6103 |
| 2 | 49.41 | 45.58 | 51.26 | B | 47.4287 |
| Delta | 1.11 | 8.78 | 2.60 | C | 55.0987 |
| Rank | 3 | 1 | 2 | D | 43.7261 |

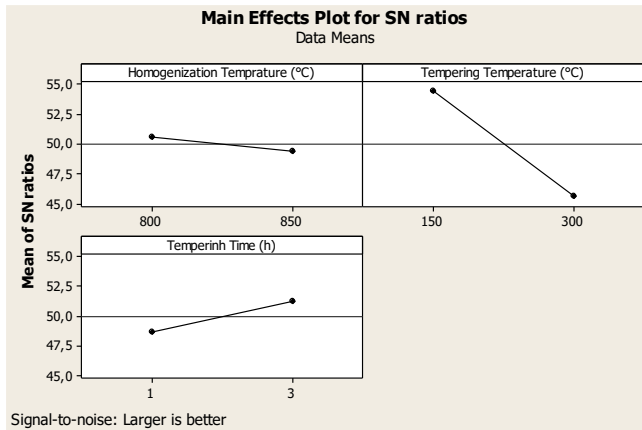


Figure 4. Mean Effects Plot for S/N ratios for hardened steel in the oil

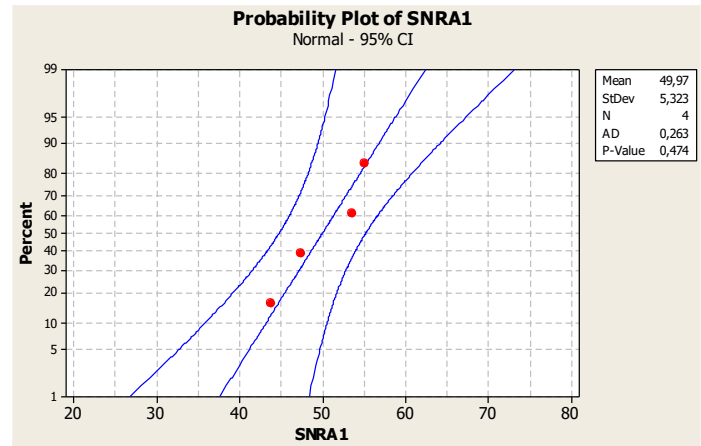


Figure 6. The probability plot for hardened steel in the oil

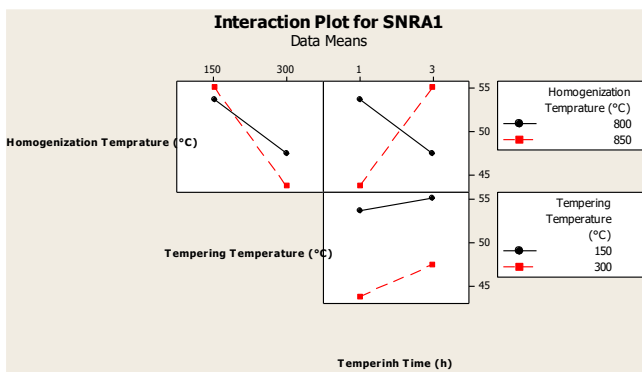


Figure 5. The interaction plot for hardened steel in the oil

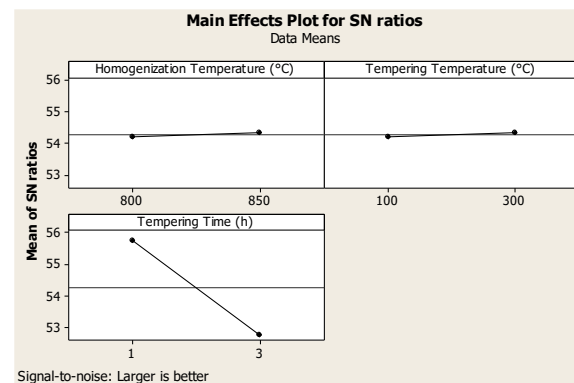


Figure 7. Mean Effects Plot for S/N ratios for hardened steel in the mixture of the oil and water

The statistical results are tabulated in Table 3. The signal (S) and noise (N) are the desirable and undesirable values. This ratio is widely used to measure the performance importance of a system. The Taguchi approach has two main advantages, i) to select the optimum level of design parameters and ii) to compare two experimental data. The highest S/N ratio value was obtained for sample C. Delta is the difference between the highest and lowest average response. Within the level 1 and 2, the highest and lowest different values are obtained at the homogenization and tempering temperatures. Rank was used to determine which factor had the largest effect. It can be seen that the tempering temperature is the most important parameter for this study. The smaller the rank for a factor has the higher the influence of the parameter on the process performance. The mean effects plot and interaction plot for S/N ratios are given in Fig. 4 and 5, respectively. It is clear from the Figure that the process changes have the different effects on the mechanical properties of the samples. The homogenization temperature affects less the hardness of samples than the tempering temperature and tempering time. In Figure 5, there is an inverse relationship between the homogenization temperature and tempering time, and a parallel relationship between the tempering temperature

and tempering time. Any change of these parameters would affect the other parameters and consequently the results.

In Fig. 6, the probability plot is displayed in the points are aligned along the line with a minimum deviation. We can see that the p-value is 0.474 and the standard deviation is 5.323, and therefore, the model is significant. To these results, the null hypothesis states that the data follow a normal distribution. Because the p-value is 0.474, which is greater than the significance level of 0.05.

The regression equation is obtained and presented for this work. The regression equation is

$$\text{Hardness (HV)} = 702 + 0.0794 \text{ Homogenization Temperature (°C)} - 2.20 \text{ Tempering Temperature (°C)} + 42.8 \text{ Tempering Time (h)}$$

The R and R² values of the results are obtained as 0.96 and 0.93, respectively. It can be said that the strength of the specimens under a given condition can be predicted to about 93% by the Taguchi method.

The statistical results for hardened steel in the mixture of the oil and water are tabulated in Table 4. The highest S/N ratio value is obtained for sample G. Within the level 1 and 2, the highest and lowest different values are obtained at the tempering

time and homogenization temperature. It can be seen that the tempering time is the most important parameter for this study.

The mean effects plot and interaction plot for S/N ratios are given in Fig. 7 and 8, respectively. The tempering time affects the hardness of samples more than the homogenization temperature and tempering temperature. In Figure 7, there is an inverse relationship between the homogenization temperature and tempering temperature, and a parallel relationship between the tempering temperature and tempering time, and between homogenization temperature and tempering time. Any change of the parameters would affect the other parameters and consequently the results.

In Fig. 9, the probability plot for hardened steel in the mixture of the oil and water is displayed. The points are aligned along the line with a minimum deviation. We can see that the p-value is 0.079 and the standard deviation is 1.712, and therefore,

the model is very significant. To these results, the null hypothesis states that the data follow a normal distribution. Because the p-value is 0.079, which is greater than the significance level of 0.05. Similarly, the tribological properties of AISI 4140 were optimized by the Taguchi method with ANOVA [34].

The regression equation for hardened steel in the mixture of the oil and water is obtained and presented for this study. The regression equation is

The hardness (HV) = 553 + 0.168 Homogenization Temperature (°C) + 0.0494 Tempering Temperature (°C) – 88.5 Tempering Time (h)

The R and R² values of the results are obtained as 0.99 and 0.99, respectively. It can be said that the hardness of the specimens under a given condition can be predicted to about 99% by the Taguchi method.

Table 4. The statistical results for hardened steel in the mixture of the oil and water

| Level | Homogenization Temperature (°C) | Tempering Temperature (°C) | Tempering Time (h) | Code | S/N ratio |
|-------|---------------------------------|----------------------------|--------------------|------|-----------|
| 1 | 54.21 | 54.20 | 55.75 | E | 55.6193 |
| 2 | 54.33 | 54.34 | 52.79 | F | 52.8031 |
| Delta | 0.11 | 0.14 | 2.96 | G | 55.8782 |
| Rank | 3 | 2 | 1 | H | 52.7738 |

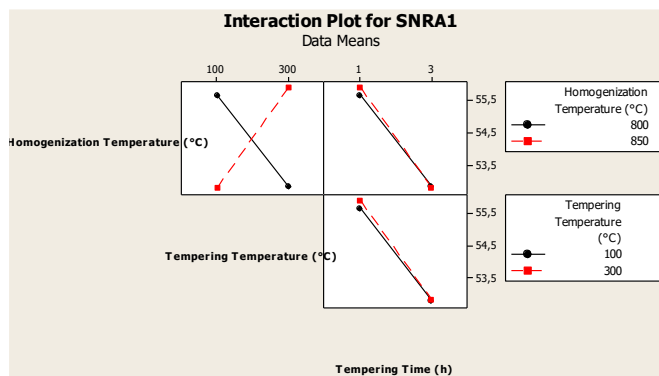


Figure 8. The interaction plot for hardened steel in the mixture of the oil and water

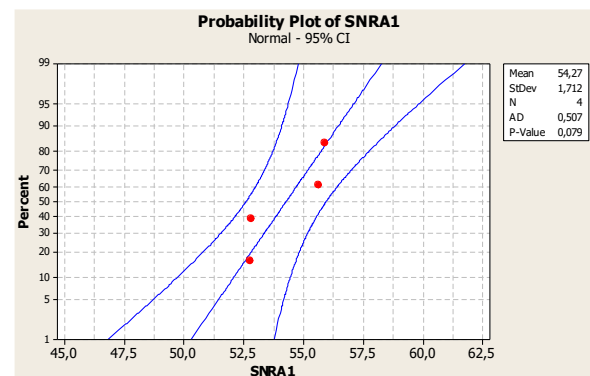


Figure 9. The probability plot for hardened steel in the mixture of the oil and water

5. Conclusion

In this study, the heat treatment process is applied to the AISI 4140 steel. The effects of the homogenization temperature, tempering temperature and tempering time on the hardness of the samples are studied. The following results can be drawn from this study.

- With increasing tempering temperature and time, the hardness values of the samples decreased. This situation is thought to be related to the phase transformation that occurs in the microstructure of AISI 4140 steel with the tempering process. The martensite structure, which has a hard structure at low tempering temperature, decreased with increasing tempering temperature and time, the grains became spherical and coarsening.
- The heat treatment process is responsible for the microstructural changes leading to the declared hardness change.
- Hardness properties of AISI 4140 are affected by the hardening media. The hardened steel in the mixture of the oil and water showed the higher hardness value than the hardened steel in the oil.

- In the DOE, the different results are obtained for each process. In the hardened steel in the mixture of the oil and water, the minimum standard deviation and p-value, and the maximum correlation and prediction ratio are observed.
- The regression equation has a high accuracy for the hardened steel in the mixture of the oil and water.

Author contributions

Halil Ibrahim Kurt: supervisor, discussion. Utku Berk Akyuz: experimental, writing. Engin Ergul: writing, control, editing.

References

1. Nayar, A., The steel handbook, Tata McGraw-Hill Publishing Company, **2002**
2. ASM International Handbook Committee, Properties and selection: nonferrous alloys and special-purpose materials, ASM International, **1992**, 2, 1143-1144
3. ASM International Handbook Committee, ASM Handbook, Properties and Selection Iron Steels and High Performance Alloys, vol. 1, **1990**

4. Gur, A.K., Ozay, C., Orhan, A., Buytoz, S., Caligulu, U., and Yigitturk, N., Wear properties of Fe-Cr-C and B₄C powder coating on AISI 316 stainless steel analyzed by the Taguchi method, *Materialpruefung/Materials Testing*, **2014**, 56(5):393–398
5. Ergul, E., Kurt, H.I., Oduncuoglu, M., Civi, C., and Eyici, G., Investigation of wear weight loss in aluminum matrix composites, **2020**, 3(2):160-170
6. Kurt, H.I., Oduncuoglu, M., and Asmatulu, R., Wear Behavior of Aluminum Matrix Hybrid Composites Fabricated through Friction Stir Welding Process, **2016**, 23(10):1119-1126
7. Ergul, E., Kurt, H.I., Civi, C., and Eyici, G., Wear Characteristics of Carbon Nanotube Reinforced Al2024 Composites, *El-Cezeri Fen ve Mühendislik Dergisi*, **2020**, 7(3):1008-1016
8. Manikonda, R.D., Kosaraju, S., Raj, K.A., and Sateesh, N., Wear Behavior Analysis of Silica Carbide Based Aluminum Metal Matrix Composites, in *Materials Today: Proceedings*, **2018**, 5(9):20104-20109
9. Totten, G.E., and MacKenzie, D.S., *Handbook of Aluminum*, in *Physical Metallurgy and Processes*, CRC press, **2003**, 1
10. Prabhudev, K.H., *Handbook of Heat Treatment of Steels*, **1988**, 1
11. ASM International Handbook Committee, *ASM Handbook, Metallography, Structures and Phase Diagrams*, vol. 8, **1973**
12. Altunpak, Y., and Akbulut, H., Al₂O₃ Kısa Fiber Takviyeli LM 13 Alüminyum Alaşımının Eğilme Dayanımına Yaşlandırma Isıl İşeminin Etkisi, *El-Cezeri Fen ve Mühendislik Dergisi*, **2019**, 6(1):175–180
13. Totten, G.E., and Howes, M.A.H., *Steel Heat Treatment Handbook*, 2nd ed. **1997**
14. Tecer, M.M., Effects of various heat treatment procedures on the toughness of AISI 4140 low alloy steel, *The International Journal of Materials and Engineering Technology*, **2020**, 3(2):131–149
15. Verma, A., and Singh, P.K., Influence of Heat Treatment on Mechanical Properties of AISI 1040 Steel, *IOSR Journal of Mechanical and Civil Engineering*, **2013**, 10(2):32–38
16. Çalığülü, U., Aras, M., and Türkmen, M., Temperleme işleminin yağda soğutulan çeliklerin mikroyapı ve sertlik özelliklerine etkisi. In *4th International Symposium on Innovative Technologies in Engineering and Science (ISITES2016)*, 3-5 Nov 2016, Antalya-Turkey, **2016**
17. Rahman, S.M.M., Karim, K.E., and Simanto, M.H.S., Effect of Heat Treatment on Low Carbon Steel: An Experimental Investigation, *Applied Mechanics and Materials*, **2016**, 860, 7–12
18. Sanij, M. K., Banadkouki, S. G., Mashreghi, A. R., and Moshrefifar, M., The effect of single and double quenching and tempering heat treatments on the microstructure and mechanical properties of AISI 4140 steel. *Materials & Design*, **2012**, 42, 339-346
19. Badaruddin, M., Wardono, H., Wang, C. J., and Rivai, A. K., Improvement of low-cycle fatigue resistance in AISI 4140 steel by annealing treatment. *International Journal of Fatigue*, **2019**, 125, 406-417
20. Kaya, A., Aslan, M., Yilmaz, N. F., and Kurt, H. I., Al-Mg-SiC Kompozitlerin Görünür Yoğunluklarının Taguchi Analizi, *El-Cezeri*, **2020**, 7(2):773–780
21. Ergul, E., and Kurt, H. I., Al Matrisli Kompozitlere ANFIS, ANN ve Taguchi Yaklaşımları Uygulanarak Özelliklerin Karşılaştırılması, *International Journal of Engineering Research and Development*, **2021**, 13(2):406–416
22. Kurt, H.I., Oduncuoglu, M., and Yilmaz, N.F., ANN in estimation shear modulus of laminate composite, *The International Journal of Materials and Engineering Technology (TIJMET)*, **2018**, 1(1):1-5
23. Kurt, H. I., and Oduncuoglu, M., Application of a Neural Network Model for Prediction of Wear Properties of Ultrahigh Molecular Weight Polyethylene Composites, *Int J Polym Sci*, **2015**
24. Rathore, S.S., Salve, M.M., and Dabhade, V.V., Effect of molybdenum addition on the mechanical properties of sinter-forged Fe-Cu-C alloys, *J Alloys Compd*, **2015**, 649, 988–995
25. Lin, H., Wang, C., Yuan, Y., Chen, Z., Wang, Q., and Xiong, W., Tool wear in Ti-6Al-4V alloy turning under oils on water cooling comparing with cryogenic air mixed with minimal quantity lubrication, *The International Journal of Advanced Manufacturing Technology*, **2015**, 81(1):87–101
26. Dhua, S.K., Mukerjee, D., and Sarma, D.S., Effect of cooling rate on the as-quenched microstructure and mechanical properties of HSLA-100 steel plates, *Metallurgical and Materials Transactions A*, **2003**, 34(11):2493–2504
27. Tavares, S. S. M., Noris, L. F., Pardal, J. M., & da Silva, M. R., Temper embrittlement of supermartensitic stainless steel and non-destructive inspection by magnetic Barkhausen noise, *Engineering Failure Analysis*, **2019**, 100, 322-328
28. Berns, H., and Theisen, W., *Ferrous materials: Steel and cast iron*, *Ferrous Materials: Steel and Cast Iron*, **2008**
29. Meysami, A.H., Ghasemzadeh, R. Seyedein, S.H., and Aboutalebi, M.R., An investigation on the microstructure and mechanical properties of direct-quenched and tempered AISI 4140 steel, *Mater Des*, **2010**, 31(3): 1570–1575
30. Lee, W.S., and Su, T.T., Mechanical properties and microstructural features of AISI 4340 high-strength alloy steel under quenched and tempered conditions, *J Mater Process Technol*, **1999**, 87(1-3):198–206
31. Chen, Y., Tam, S., Chen, W.L., and Zheng, H.Y., Application of the Taguchi method in the optimization of laser micro-engraving of photomasks, *International Journal of Materials & Product Technology*, **2014**
32. Thakur, A., Rao, T., Mukhedkar, M., and Nandedkar, V., Application of Taguchi method for resistance spot welding of galvanized steel, **2010**
33. Adin, M.S., and Iscan, B., Optimization of process parameters of medium carbon steel joints joined by MIG welding using Taguchi method, *European Mechanical Science*, **2022**, 6(1):17–26
34. Rooprai, R.S., Singh, H., Singh, T., and Singla, Y.K., Analysis of the wear properties of through hardened AISI-4140 alloy steel using Taguchi technique, *Mater Today Proc*, **2022**, 50, 661–664

RESEARCH ARTICLE

Validation of material model and mechanism of material removal in abrasive flow machining

Omer Eyercioglu¹, Kursad Gov² and Adem Aksoy³¹Gaziantep University, Faculty of Mechanical Engineering, Department of Mechanical Engineering, Gaziantep, Türkiye²Gaziantep University, Faculty of Aeronautics and Astronautics, Aerospace Engineering Department, Gaziantep, Türkiye³Gaziantep Islam Science and Technology University, Vocational School of Technical Sciences, Gaziantep, Türkiye

Article Info

Article history:

Received: 18.01.2023

Revised: 12.05.2023

Accepted: 24.05.2023

Published Online: 26.05.2023

Keywords:

Abrasive flow machining

Surface finishing

Mathematical modeling

CFD analysis of AFM

Abstract

Abrasive flow machining (AFM) is a non-traditional surface finishing method that is recently becoming popular. Increasing surface quality demands and developing manufacturing technologies need high costs and time. AFM process satisfies these demands in a short time period. In this study, the material removal model for a double-acting AFM and the experimental validation of the model was presented. The material removal model was based on the previously performed mathematical studies and the active grain numbers and the total material removal formulations were re-evaluated. A CFD analysis was carried out to determine the wall shear stress, velocity distribution, static and dynamic pressure values and used in the mathematical model. The experimental study is performed on the Ti-6Al-4V alloy using 400 mesh size SiC abrasive for 20%, 40%, and 60% abrasive concentrations by weight. The results of the experimental study were compared with the results of the mathematical model presented in the study. The differences between the results of the presented model and the experimental ones are very close to each other for all abrasive concentrations. By using the presented model, the AFM process parameters can be pre-determined according to the required final form.

1. Introduction

Abrasive flow machining (AFM) is a non-traditional finishing method that is recently becoming popular [1-4]. AFM method is successfully applied to medical, aerospace, and other precision manufacturing areas [5]. Increasing surface quality demands and developing manufacturing technologies need high cost and time. AFM process satisfies these demands in a short time period [6]. In the AFM method, complex geometries and difficult-to-reach surfaces can be processed more easily than traditional methods [7, 8].

The AFM process is performed by extrusion of the polymeric media between two reciprocating pistons in cylinders (Figure 1). The polymeric media contains abrasive particle, hydraulic oil, water, and a polymeric material. Media flows through the surface of the workpiece at high pressure [9]. The surface is getting smoother and cleaner after AFM process [6]. This process is effective for mostly the parts manufactured by wire electrical discharge machined (WEDM) surfaces [10].

Types of workpiece materials and material properties influence surface roughness after the AFM process [11]. The studies which are experienced on Ti-6Al-4V [12, 13] and AISI D2 hardened tool steel show that AFM process has better results on harder materials [14, 15]. The residual asperities are getting smoother or entirely removed without any change in geometry by AFM method [16]. Viscosity, abrasive concentration, abrasive type, and mesh size are effective parameters in the process. Abrasive media generally includes abrasive particles as silicon carbide (SiC) particles [17, 18]. Besides, aluminum oxide, boron carbide, or garnet are used as an abrasive particle.

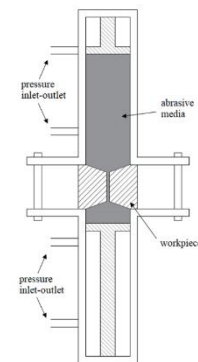


Figure 1. Abrasive Flow Machine (AFM) model

Jain et. al. [19] examined the AFM media parameters and showed that the viscosity of media is proportional to the temperature, concentration and mesh size of the abrasive. Media viscosity is directly proportional to the abrasive concentration and inversely proportional to the abrasive mesh and temperature. In addition, they found that higher viscosity results in higher material removal and improved surface quality.

Modeling is conventionally an effective method to design and analyze a process or a product and it is considered beneficial while designing improvements for increasing process performances. In the late 1980s, many efforts were done to a material removal mechanism and surface generation modeling of the AFM operation [20]. For the analysis of flow, computational fluid dynamics (CFD) is one of the most popular simulation methods. Widely used analysis tools such as ANSYS FLUENT have been preferred by various researchers [21].

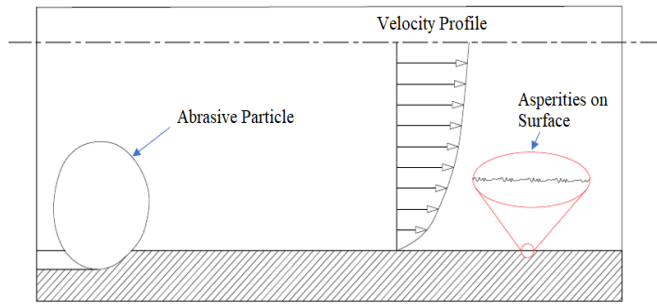


Figure 2. Material removing model

Rajeshwar et. al [22] carried out modeling and simulation studies of the AFM process. They used primary equations of the Maxwell model to define the non-newtonian flow characteristics of the AFM media for the cylindrical workpiece. In another study, the interaction between workpieces and abrasive particles was examined [23]. They have shown that a higher concentration of abrasives produces better surfaces and higher material removal. The finite element method was used to determine the velocity and stress distribution in the AFM process [24]. The velocity and pressure distribution inside the flow geometry can be obtained from CFD simulation. The velocity is maximum at the center and minimum near the walls. The pressure decreases gradually after passing from the inlet to the exit [25].

In this study, the material removal model for a double-acting AFM and the experimental validation of the model was presented. The material removal model was based on the mathematical model suggested by Jain et.al [4] and the active grain numbers and the total material removal formulations were re-evaluated. The experimental study was performed on the Ti-6Al-4V alloy using 400 mesh size SiC abrasive material for abrasive concentrations of 20%, 40% and 60% by weight. A CFD analysis was carried out to determine the wall shear stress, velocity distribution, static and dynamic pressure values and used in the mathematical model. The amount of metal removal from the workpiece surface was investigated at different abrasive concentrations. The results of the experimental study that was previously done for Ti-6Al-4V alloy [26] were compared with the results of the mathematical model presented in this study.

2. The mechanism of material removal and the mathematical model

2.1 The mechanism of material removal

In the AFM process, the material removals occur by the motion of the particles (Figure 2). Particle size and shapes are different but all particles assumed as circular or near-circular shaped in the modeling. The particles are near the surface of the workpiece called active particles. Active particles remove the surface of the workpiece (Figure 3).

2.2. The Mathematical Model of the Material Removal

The material removal model is based on the mathematical model suggested by Jain et.al [13]. The active grain numbers and the total material removal formulations were re-evaluated.

The force (F) acting on the abrasive grain produces an indentation and the plastically deformed zone rises upward. When the media flows through the surface at high pressure, the abrasive grain shears the plastically displaced material and forms a chip. To obtain the actual diameter of the abrasive from mesh size to millimeter:

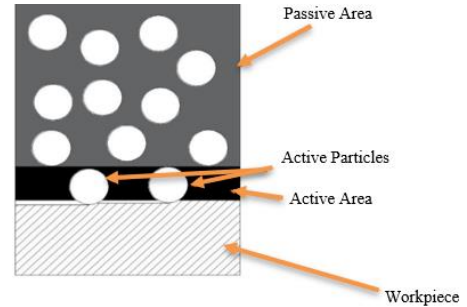


Figure 3. Active and passive areas-particles

$$d_g = \frac{28}{M^{1.1}} \quad (1)$$

The vertical force component (indenting force) on the grain with a diameter (d_g) is calculated by

$$F = \sigma \frac{\pi d_g^2}{4} \quad (2)$$

where σ is wall shear stress acts on the abrasive grain. Taking a as the radius of the indentation projected area (ΔA), and H_w as the workpiece material hardness, the force can be expressed as:

$$F = H_w \Delta A = H_w \pi a^2 \quad (3)$$

The indentation depth (t) and the radius (a) can be obtained from Figure 4 as:

$$a = \sqrt{\frac{F_r}{H_w \pi}} \quad (4)$$

$$t = \frac{d_g}{2} - \sqrt{\left(\frac{d_g^2}{4} - r_a^2\right)} \quad (5)$$

and

$$a = \sqrt{t(d_g - t)} \quad (6)$$

The indentation depth (t) is finally expressed by substituting a from Eqn. (4) into Eqn. (5);

$$t = \frac{d_g}{2} - \sqrt{\left(\frac{d_g^2}{4} - \frac{F_n}{H_w \pi}\right)} \quad (7)$$

where, F_n is normal force applied to abrasive grain, t is depth of indentation of abrasive into workpiece material, H_w is hardness of workpiece material and d_g is diameter of abrasive grain. Similarly, angle θ can be calculated using the triangle ΔOAB shown in Figure 4(b);

$$\theta = \sin^{-1} \left(\frac{2a}{d_g} \right) \quad (8)$$

The generated cross-sectional area of the groove (A_g) which is the hatched area of the grain in Figure 4(a) is the difference between the areas of sector $OADCO$ and triangle ΔAOC .

$$A_g = \pi \frac{d_g^2}{2} \left(\frac{\theta}{2\pi} \right) - \frac{1}{2} 2a \left(\frac{d_g}{2} - t \right) \quad (9)$$

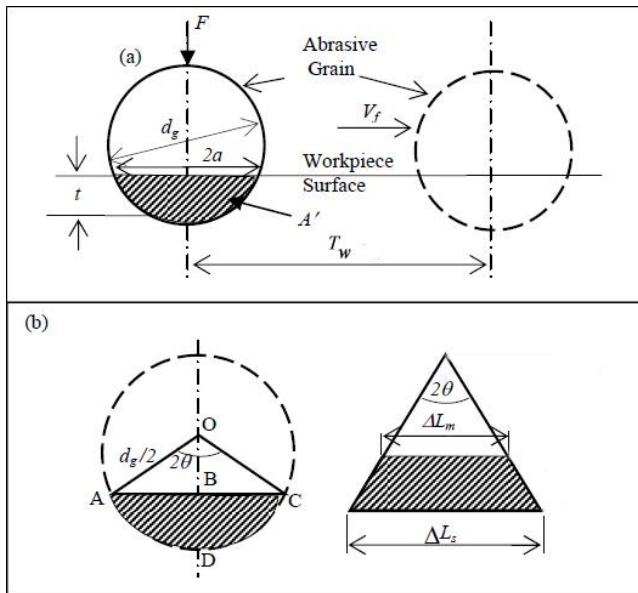


Figure 4. (a) Spherical representation of abrasive grain
(b) Triangular asperity model of the workpiece surface [13]

By substituting a and θ from Eqns. (6) and (8), (A_g) is found as;

$$A_g = \frac{d_g^2}{4} \sin^{-1} \frac{2\sqrt{t(d_g-t)}}{d_g} - \sqrt{t(d_g-t)} \left(\frac{d_g}{2} - t \right) \quad (10)$$

Then the material removed by weight (W_a) by an abrasive grain is;

$$W_a = \rho A_g T_w \quad (11)$$

where T_w is the workpiece width. By substituting A_g into Eqn. (11),

$$W_a = \rho \left[\frac{d_g^2}{4} \sin^{-1} \frac{2\sqrt{t(d_g-t)}}{d_g} - \sqrt{t(d_g-t)} \left(\frac{d_g}{2} - t \right) \right] T_w \quad (12)$$

Assuming that all active grains behave similarly, the total material removal is the multiplication of the number of active grains (N_a) by W_a . The number of active grains (N_a) per unit length is;

$$N_a = \frac{C}{d_g} \quad (13)$$

where C is the abrasive media concentration by weight. From this, total number of abrasive grains acting to surface of workpiece (N_s) is equal to

$$N_s = S N_a L_m \quad (14)$$

Length of the media (L_m) can be calculated from the rate between areas cylinder and slot cross-section. S is workpiece contour length and T_s is slot thickness of passage which media passes.

$$L_m = \frac{\pi R_c^2 L_s}{S T_s} \quad (15)$$

where, L_s is stroke length and R_c is radius of media cylinder. Hence, the weight of material removed in a single stroke (W) of the AFM process is derived as;

$$W = W_a N_s \quad (16)$$

Total weight of material removal (W_t) can be found by multiplying the number of cycles (n)

$$W_t = nW \quad (17)$$

$$W_t = n \times \rho \left[\frac{d_g^2}{4} \sin^{-1} \frac{2\sqrt{t(d_g-t)}}{d_g} - \sqrt{t(d_g-t)} \left(\frac{d_g}{2} - t \right) \right] T_w \times S N_a L_m \quad (18)$$

According to this model, the material removal depends on the indentation depth (t), the abrasive grains size (d_g), and the number of abrasive grains (N_s) acting on the working area of the workpiece.

2.3. The CFD Model

ANSYS FLUENT was used for analyzing the process. By using the results of the analysis the wall shear stress, velocity distribution, and static and dynamic pressure values can be determined and used in the mathematical model. The workpiece model has a rectangular flow passage (2mmx20mmx10mm) as shown in Figure 5.

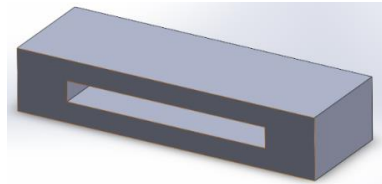


Figure 5. Workpiece mode



Figure 6. Two-way abrasive flow machine

3. Experimental Study

The experimental study was performed on a two-way AFM machine which was shown in Figure 6. The Ti-6Al-4V alloy samples were cut by using wire-EDM to 5x10x20 mm prisms from a stock (Figure 7). The samples were weighed by using

Shimadzu Aux220 balance before and after the AFM process. A polymer-based abrasive media was prepared using 400 mesh sizes of SiC abrasives with weight concentrations of 20%, 40%, and 60%. The media and the process parameters were given in Table 1.



Figure 7. Ti-6Al-4V alloy samples

4. Results and Discussion

The CFD analysis was carried out by using ANSYS FLUENT and the results were shown in Figure 8. The wall shear stress is 0.517 MPa for the flow geometry. The material removal carried out using 400 mesh size SiC abrasive for abrasive concentrations of 20%, 40%, and 60% by weight. The results of the experimental study were compared with the results of the mathematical model presented in this study. The comparison of the mathematical and experimental material removal can be seen in Figure 9 for various AFM cycles.

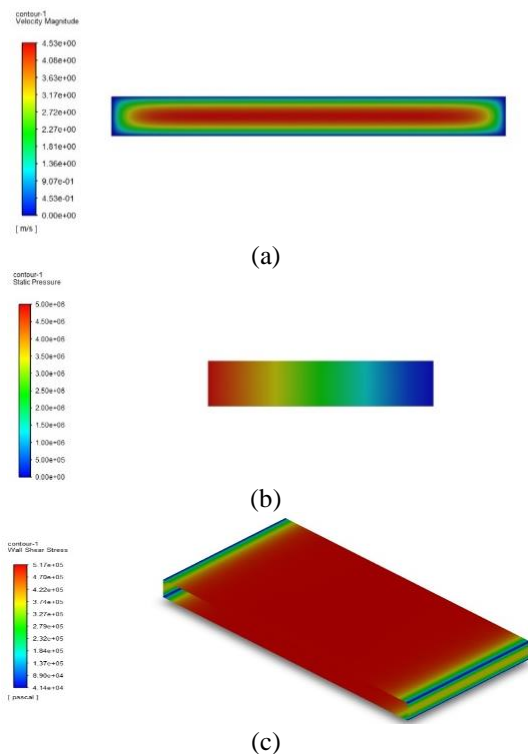
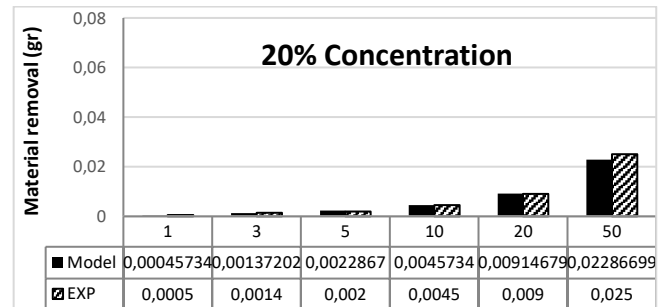


Figure 8. The results of CFD analysis a) velocity b) static pressure and c) wall shear stress distributions.

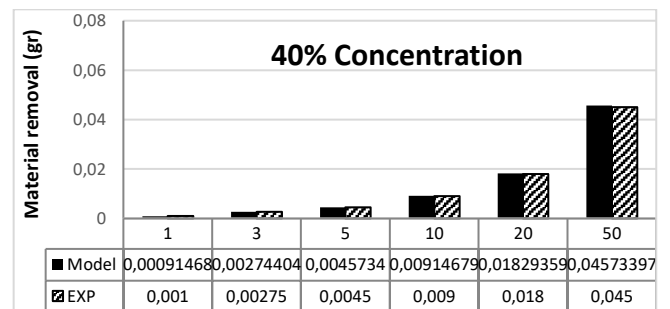
The amount of material removal is increasing with the increasing abrasive concentration. It can be clearly seen in the figures. The difference between the results of the presented model and experimental ones are very close to each other for all abrasive concentrations. With a help of the presented model, material removal can be pre-determined before the AFM process. In the material model; the media viscosity, the workpiece material hardness, the area of the passage, abrasive grain size, and wall shear stress value are the main dependent values that affect the system. Therefore, the model needs to be verified for other parameters (i.e. viscosity of media, the hardness of workpiece material, area of the passage, and abrasive grain size) also.

Table 1. The AFM media and the process parameters

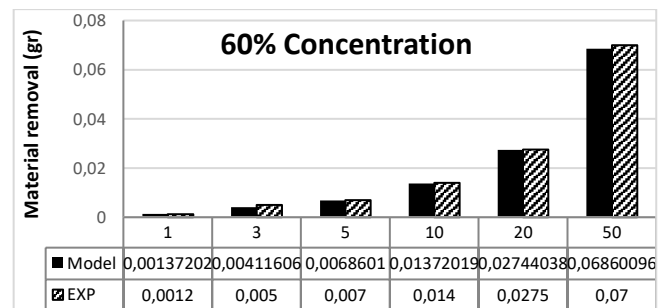
| Parameter | Value |
|----------------------------------|-------------------------|
| Number of cycles | 1, 3, 5, 10, 20, 50 |
| Abrasive type | SiC |
| Abrasive mesh size | 400 |
| Abrasive media | Polymer based |
| Abrasive concentration | 20%, 40%, 60 % wt. |
| Abrasive media speed | 400 mm/min |
| Abrasive media viscosity | 60 Pa.s |
| Abrasive media flow per cycle | 6 liters per 90 seconds |
| Working pressure | 5 MPa |
| Bore diameter of the AFM machine | 140 mm |
| Stroke length of the AFM machine | 400 mm |



(a)



(b)



(c)

Figure 9. The material removal results predicted by the mathematical model and the experimental study with respect to AFM cycles for a) 20% b) 40% and c) 60% abrasive concentrations.

5. Conclusions

In conclusion, the mathematical model which was derived to obtain material removal can be successfully used for the AFM process design. By using the presented model, the AFM process parameters can be pre-determined according to the required final form. The model was verified for different abrasive concentrations for a constant set of other AFM parameters. The model needs to be verified for other parameters (i.e. viscosity of media, the hardness of workpiece material, area of the passage, abrasive grain size) in further studies.

Acknowledgments

The authors would like to acknowledge the contributions of the Scientific Project Bureau (BAPYB) of The Gaziantep University.

Author contributions

All authors contributed to the study conception and design. Omer Eyercioglu performed the project administration, review and editing. Kursad Gov performed the first draft of the manuscript, validation and analysis. Adem Aksoy performed the material preparation, data collection and visualization. All authors commented on previous versions of the manuscript and read and approved the final manuscript.

References

- Kumar, S.S., Hiremath, S.S., A review on abrasive flow machining (AFM), *Procedia Technology*. **2016**, 25:1297-1304
- Dixit, N., Sharma, V., and Kumar, P., Research trends in abrasive flow machining: A systematic review, *Journal of manufacturing Processes*. **2021**, 64:1434-1461
- Rhoades, L., Abrasive flow machining: a case study, *Journal of Materials Processing Technology*. **1991**, 28(1-2):107-116
- Jain, R.K., Jain, V.K., and Dixit, P., Modeling of material removal and surface roughness in abrasive flow machining process, *International Journal of Machine Tools and Manufacture*. **1999**, 39(12):1903-1923
- Jain, R.K., Jain, V.K., Specific energy and temperature determination in abrasive flow machining process, *International Journal of machine tools and manufacture*. **2001**, 41(12):1689-1704
- Jain, V., Adsul, S., Experimental investigations into abrasive flow machining (AFM), *International Journal of Machine Tools and Manufacture*. **2000**, 40(7):1003-1021
- Li, J., Zhu, Z., Hu, J., Zhou, Z., Zhang, X., and Zhao, W., Particle collision-based abrasive flow mechanisms in precision machining, *The International Journal of Advanced Manufacturing Technology*. **2020**, 110:1819-1831
- Munhoz M.R., Dias, L.G., Breganon, R., Ribeiro, F.S.F., de Souza Gonçalves, J.F., Hashimoto, E.M., and da Silva Júnior, C.E., Analysis of the surface roughness obtained by the abrasive flow machining process using an abrasive paste with oiticica oil, *The International Journal of Advanced Manufacturing Technology*. **2020**, 106(11-12):5061-5070
- Eyercioglu, Ö, Göv, K., and Aksoy, A., Abrasive Flow Machining Of Asymmetric Spur Gear Forging Die, *Harran Üniversitesi Mühendislik Dergisi*. **2018**, 4(1):12-20
- Göv, K., Eyercioglu, Ö., Abrasive Flow Machining of Ti-6Al-4V. in *International Science and Technology Conference*. of Conference. **2017**
- Kopač, J., Bahor, M., Interaction of the technological history of a workpiece material and the machining parameters on the desired quality of the surface roughness of a product, *Journal of Materials Processing Technology*. **1999**, 92:381-387
- Inagaki, I., Takechi, T., Shirai, Y., and Ariyasu, N., Application and features of titanium for the aerospace industry, *Nippon steel & sumitomo metal technical report*. **2014**, 106(106):22-27
- Narutaki, N., Murakoshi, A., Motonishi, S., and Takeyama, H., Study on machining of titanium alloys, *CIRP Annals*. **1983**, 32(1):65-69
- Gov, K., Eyercioglu, O., Effects of abrasive types on the surface integrity of abrasive-flow-machined surfaces, *Proceedings of the Institution of Mechanical Engineers, Part B: Journal of Engineering Manufacture*. **2018**, 232(6):1044-1053
- Gov, K., Eyercioglu, Ö., and Çakır, M., Investigation of the Effect of Abrasive Flow Machining (AFM) Parameters on Wire Erosion Cut Die Surface, *TMMOB Chamber of Mechanical Engineers Konya Branch VI. Machinery Design and Manufacturing Technologies Congress*. **2011**
- Aksoy, A., Eyercioglu, O., and Gov, K., Abrasive Flow Machining Of Fiber Extrusion Spinneret Holes. in *The International Conference of Materials and Engineering Technology (TICMET'19)*. of Conference. Gaziantep Turkey **2019**
- Bremerstein, T., Potthoff, A., Michaelis, A., Schmiedel, C., Uhlmann, E., Blug, B., and Amann, T., Wear of abrasive media and its effect on abrasive flow machining results, *Wear*. **2015**, 342:44-51
- Sudhakara, D., Suresh, S., and Vinod, B., Experimental study on Abrasive Flow Machining (AFM): new approach for investigation on Nano-SiC in the improvement of material removal and surface finishing, *Journal of Bio-and Tribo-Corrosion*. **2020**, 6(1):24
- Jain, V., Ranganatha, C., and Muralidhar, K., Evaluation of rheological properties of medium for AFM process, **2001**,
- Williams, R.E., Rajurkar, K., Metal removal and surface finish characteristics in abrasive flow machining, *Mechanics of Deburring and Surface Finishing Processes*. Presented At The Winter Annual Meet. of The American Soc. Mechanical. **1989**, 38:93-106
- Gedik, E., Kurt, H., Recebli, Z., and Balan, C., Two-dimensional CFD simulation of magnetorheological fluid between two fixed parallel plates applied external magnetic field, *Computers & fluids*. **2012**, 63:128-134
- Rajeshwar, G., Kozak, J., and Rajurkar, K.P., Modelling and monitoring and control of abrasive flow machining. in *Proc. of NSF Design and Manufacturing system conference*. of Conference. **1994**
- Jain, R.K., Jain, V.K., Simulation of surface generated in abrasive flow machining process, *Robotics and Computer-Integrated Manufacturing*. **1999**, 15(5):403-412
- Singh, S., Shan, H., Development of magneto abrasive flow machining process, *International Journal of Machine Tools and Manufacture*. **2002**, 42(8):953-959
- Seifu, Y., Kumar, S.S., and Hiremath, S.S., Modeling and simulation: machining of mild steel using indigenously developed abrasive flow machine, *Procedia Technology*. **2016**, 25:1312-1319
- Soydan, O., Gov, K., and Eyercioglu, O., Surface Finishing of Aerospace Materials, *El-Cezeri Journal of Science and Engineering*. **2020**, 7(2):700-709

RESEARCH ARTICLE

Variation of magnetic properties in strontium magnet powders with Sr/Fe ratio

Sümran Bilgin^{*1} , Sultan Öztürk¹  and Kürşat İçin¹ ¹Karadeniz Technical University, Engineering Faculty, Metallurgical and Materials Department, Trabzon, Türkiye

Article Info

Article history:

Received: 20.04.2023

Revised: 01.06.2023

Accepted: 02.06.2023

Published Online: 08.06.2023

Keywords:

Mechanochemical synthesis

Strontium hexaferrite

Magnetic properties

Sr/Fe ratio

Abstract

The aim of our current study was to investigate the impact of Sr/Fe ratio on both the phase formation and magnetic properties of strontium hexaferrite powders. To achieve this, we employed mechanochemical synthesis to synthesize the powders, followed by a heat treatment process at 950°C for a period of 1 hour under an open atmosphere. XRD patterns revealed that the primary phase in all powders was identified as the SrFe₁₂O₁₉ phase. The SEM image showed that the particles had a round morphology with partial agglomeration due to the reduction in particle size. The magnetic properties were found to be affected by Sr/Fe ratio. The (BH)_{max} values increased from 0.35 MGOe to 3.11 MGOe as the Sr/Fe increased from 1:11.0 to 1:12.0. The presence of secondary phases such as α-Fe₂O₃ and SrO weakened the magnetic properties. The weight fraction of the SrO phase increased with a decrease in stoichiometry from 1:12 to 1:11, which correlated with the weakening of the magnetic properties. The study concludes that the Sr/Fe ratio between Sr/Fe is a critical parameter in determining the magnetic properties of strontium hexaferrite powders.

1. Introduction

Strontium hexaferrite (SrM), also known as SrFe₁₂O₁₉, is a type of magnetic material that belongs to the family of ferrites. It is a highly anisotropic material with high magnetic anisotropy and exhibits excellent magnetic properties such as high coercivity, high magnetic moment, and low magnetic damping [1-3]. These properties make it an attractive material for various magnetic applications, including data storage, magnetic sensors, microwave devices, and permanent magnets [4, 5].

Strontium hexaferrite magnets are composed of a combination of strontium sulfate and iron oxide, which are sintered at high temperatures to form a ceramic material. The unique crystal structure of strontium hexaferrite gives it its magnetic properties. It has a hexagonal crystal structure, with a space group of P6₃/mmc, and consists of layers of iron oxide with strontium ions in between [6]. The layers are stacked in a way that creates a uniaxial magnetic anisotropy, which makes strontium hexaferrite magnets highly resistant to demagnetization [7].

Strontium hexaferrite magnets are commonly used in various applications that require strong permanent magnets, such as speakers, electric motors, generators, and magnetic separators. They are also used in microwave devices such as circulators, isolators, and phase shifters, where their low magnetic damping and high coercivity are advantageous [8, 9]. Furthermore, they are used in magnetic recording media such as magnetic tapes and hard disk drives due to their high magnetic moment and thermal stability [10].

The basic production process for sintered strontium hexaferrite magnets involves the traditional powder metallurgy method. In this method, different types of strontium hexaferrite powders produced using various techniques are subjected to

classification, pressing, and sintering processes to produce the sintered magnets. The techniques used to produce SrM magnet powders include traditional ceramic methods, mechanochemical synthesis, self-propagating high-temperature synthesis, co-precipitation, sol-gel, hydrothermal synthesis, spray pyrolysis, molten salt and Pechini methods [11-16]. These methods involve different chemical and physical processes to produce strontium hexaferrite powders, which are then used to manufacture high-quality sintered magnets for various industrial applications [17]. Tiwary et al. [18] utilized celestite and iron ore powders in their research for the preparation of strontium hexaferrite powder. The powder produced through the annealing process was sintered at 1250 °C for 1 hour to produce SrM magnets. As a result of these experimental studies, the maximum coercivity was determined to be approximately 270 kA/m (3390 Oe) after a synthesis time of 50 hours. In their research, Tiwary and Narayan utilized celestite (natural strontium ore) and tuff as raw materials for the preparation of strontium hexaferrite powder. They stated that a single-phase structure was achieved through 40 hours of mechanochemical synthesis, followed by annealing at 900 °C. The magnetic properties obtained for this synthesis time and annealing temperature were as follows: 2533 Gauss remanence, 3160 Oe coercivity, and 1.19 MGOe energy product [19]. F. Sánchez-De Jesús and colleagues produced M-type strontium hexaferrite from mechanically activated strontium and iron oxides through a high-energy milling process for 5 hours. The aim of their study was to investigate the differences between the traditional heat treatment and spark plasma sintering (SPS) methods in sintering the produced hexaferrite powders at relatively low temperatures (900 °C). The magnetic properties of the hexaferrites produced using both methods varied between H_c = 288-509 kA/m and B

Corresponding Author: Sümran Bilgin
E-mail: sumranbilgin@ktu.edu.tr

How to cite this article:

Bilgin, S., Öztürk, S., and İçin, K., Variation of magnetic properties in strontium magnet powders with Sr/Fe ratio, The International Journal of Materials and Engineering Technology (TIJMET), 2023, 6(1): 12-15

= 0.29-0.32 T. They stated that these magnetic properties were consistent with the permanent magnet values of nanostructured $\text{SrFe}_{12}\text{O}_{19}$ synthesized using other methods [20]. Luo prepared Sr-ferrite powders using SrCO_3 and Fe_2O_3 as raw materials through a mechanochemical synthesis process. The saturation magnetization of the annealed powders was measured to be 58.2 Am²/kg at room temperature, with a coercivity value of 281.2 kA/m. Luo stated that compared to the traditional ceramic method, the mechanochemical method provided the advantage of achieving a higher coercive field (coercivity) [21].

The objective of this study was to utilize the mechanochemical synthesis (MCS) production technique for the production of strontium hexaferrite magnets with a hexagonal crystal structure. By employing the MCS method, SrM powders were generated by altering the Sr/Fe ratio using SrSO_4 and Fe_2O_3 . The Sr/Fe ratio was systematically varied from 1:11 to 1:12.0 with a 0.1 increment in order to investigate the influence of this ratio on the magnetic properties. The findings of the study demonstrated that the magnetic properties of the SrM magnets were notably influenced by the Sr/Fe ratio.

2. Materials and methods

Strontium hexaferrite ($\text{SrFe}_{12}\text{O}_{19}$) particles were produced by utilizing SrCO_3 as the source of Sr and mill scale, a by-product of mild steel production, as the source of Fe. Initially, the mill scale was purified by washing it with distilled water and then drying it at 100°C for 8 hours. Next, the milled mill scale was heat-treated at 900°C for 2 hours in atmospheric conditions to convert FeO and Fe_3O_4 phases to Fe_2O_3 . The Sr/Fe amounts of Fe_2O_3 and SrCO_3 were mixed and subjected to a mechanochemical synthesis process through high-energy ball milling for 20 minutes. The SrCO_3 and Fe_2O_3 powder mixture had a different Sr/Fe ratio range of 1:11 to 1:12.

The SrCO_3 and Fe_2O_3 powders, along with 10 mm WC balls and 1.2 ml of ethanol as a process control agent, were combined and loaded into a 250 ml WC milling jar. The milling process was performed in air at ambient temperature, using a fixed rotating speed of 420 rpm and a ball to powder weight ratio of 10:1 for a duration of 25 minutes. Following the high-energy ball milling process, the synthesized powders were heat-treated at 950 °C for 1 hour in order to stabilize their crystalline structure, which may have degraded during the mechanochemical synthesis process. Zeiss brand LS 10 model scanning electron microscope (SEM) was used to morphological analysis. The crystalline phases of the samples were identified through XRD measurements using a PANalytical X'pert Powder³ X-ray diffractometer. The patterns were collected in the range of 20-60° and a time per step of 180. The percentages of different phases of the powders were determined using Rietveld refinement analysis. Magnetization studies were conducted at room temperature using a LDJ Electronics 9600 vibrating sample magnetometer (VSM).

3. Results and discussion

SEM image (in Figure 1) revealed that the particles synthesized using a 1:12.0 Sr/Fe ratio and a 200-minute mechanochemical synthesis process displayed a round morphology, with some partial agglomeration observed due to the reduction in particle size. Most of the particles were around 1 μm in size, with only a small number of particles larger than 3 μm detected. The XRD patterns of $\text{SrFe}_{12}\text{O}_{19}$ powders synthesized with Sr/Fe ratios ranging from 1:11 to 1:12.0, with an increment of 0.2, are shown in Figure 2. The primary phase

in all powders was identified as the $\text{SrFe}_{12}\text{O}_{19}$ phase by their XRD patterns, and the phase peaks of $\text{SrFe}_{12}\text{O}_{19}$ belonged to the hexagonal magnetoplumbite structure with a space group of P63/mmc, as determined by HighScore Plus software. The lattice parameters of the hexagonal crystal structure were calculated to be $a=b=5.88 \text{ \AA}$ and $c=23.06 \text{ \AA}$ for the 1:12 Sr/Fe ratio. The increase in the c lattice parameter is attributed to the presence of elements in the mill scale structure.

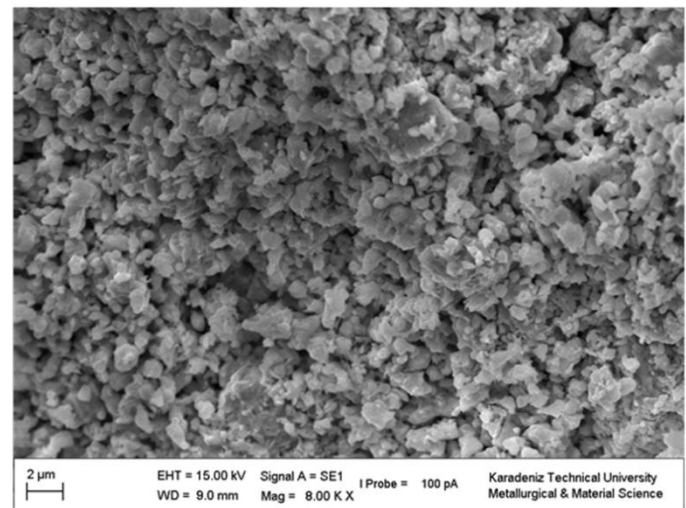


Figure 1. SEM image of strontium hexaferrite ($\text{SrFe}_{12}\text{O}_{19}$) powders after 200 minutes of mechanochemical synthesis

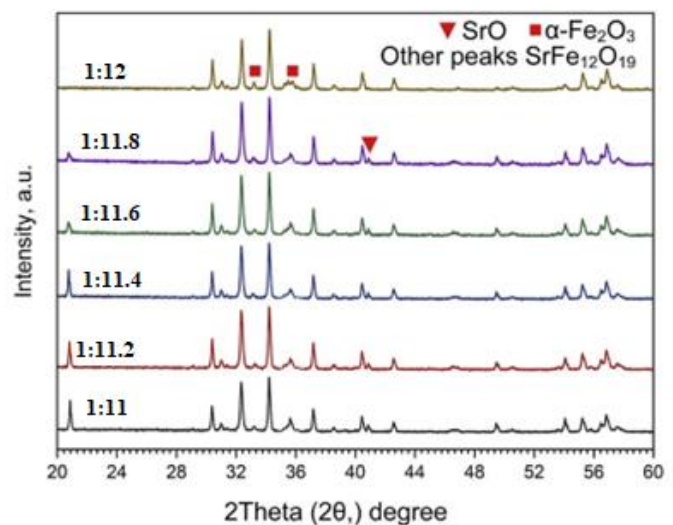


Figure 2. X-ray diffraction patterns (XRD) of mixtures with different Sr:Fe ratios

Strontium hexaferrite ($\text{SrFe}_{12}\text{O}_{19}$) is a well-known hard magnetic material with industrial applications, such as in magnetic data storage devices, microwave devices, and sensors. In this study, the effects of Sr/Fe ratios on the phase formation and magnetic properties of strontium hexaferrite powders synthesized by synthesis and heat treated at 950°C for 1 hour under an open atmosphere were investigated.

The results showed that the Sr/Fe ratio between SrCO_3 and Fe_2O_3 had a significant effect on the phase formation and magnetic properties of the synthesized strontium hexaferrite powders. When the Sr/Fe ratio was below the theoretical value of 1:12, $\alpha\text{-Fe}_2\text{O}_3$ and SrO phases formed in addition to the $\text{SrFe}_{12}\text{O}_{19}$ phase. The weight fraction of the SrO phase was

found to increase with a decrease in stoichiometry from 1:11.8 to 1:11, which explained the weakening magnetic properties.

The hysteresis loops of the synthesized powders were obtained, and magnetic properties such as coercivity (H_c), magnetic flux density (B_s), residual magnetic flux density (B_r), and maximum energy product ($(BH)_{max}$) were calculated. The results showed that as the Sr/Fe ratio increased from 1:11 to 1:12.0, the values of H_c , B_s , and B_r also increased. The $(BH)_{max}$ values, which are an indicator of the strength of a magnet, were obtained as 3.11, 2.36, 2.35, 0.4, 0.4, and 0.35 MGOe, respectively. It is noteworthy that the formation of the SrO phase increases as the Sr/Fe ratio decreases from 1:12 to 1:11. The weight fraction of this phase was found to increase from 1.6% to 7.4%, which correlates with the observed weakening of the magnetic properties. It is likely that the presence of the SrO phase interferes with the formation and alignment of the hard magnetic phase, resulting in weaker magnetic properties.

The formation of a "kink" in the hysteresis loop was observed in almost all samples, which was particularly prominent in the sample with a Sr/Fe ratio of 1:11. This shape distortion was reported to be due to the presence of secondary phases such as α - Fe_2O_3 and SrO, which are not the hard magnetic phase ($SrFe_{12}O_{19}$) present in the structure, or differences in particle size. Kink formation due to transitions between hard and soft magnetic phases or paramagnetic phases in the structure of any magnetic material was also observed. In conclusion, the Sr/Fe ratio between $SrCO_3$ and Fe_2O_3 plays a critical role in the phase formation and magnetic properties of strontium hexaferrite powders synthesized by mechanochemical synthesis and heat-treated at $950^\circ C$ for 1 hour under an open atmosphere. The results showed that as the Sr/Fe ratio increased, the magnetic properties improved, while the presence of secondary phases such as α - Fe_2O_3 and SrO weakened the magnetic properties. These findings can be useful for the optimization of the synthesis conditions and the development of high-performance magnetic materials.

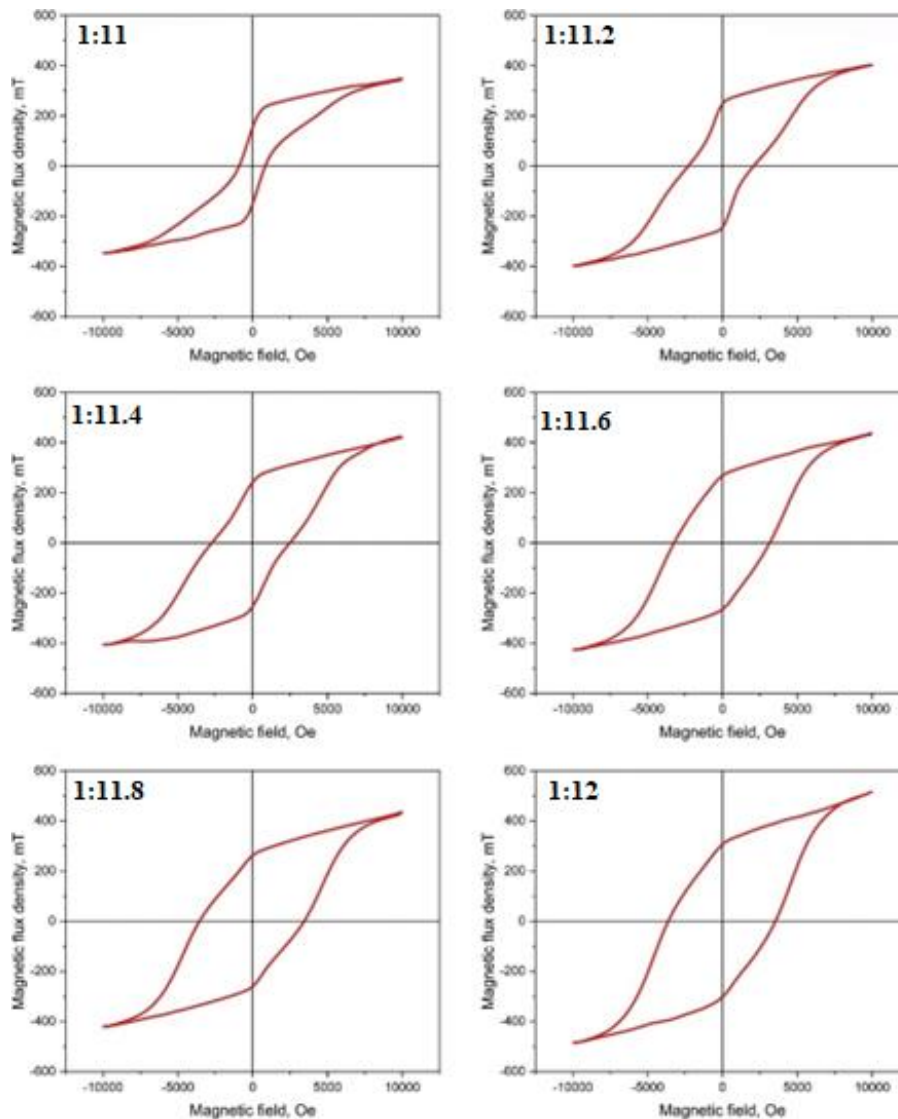


Figure 3. Magnetic hysteresis loops of produced hexaferrite powders

4. Conclusions

Based on the results of this study, it can be concluded that the Sr/Fe ratio between $SrCO_3$ and Fe_2O_3 is a critical parameter in determining the phase formation and magnetic properties of

strontium hexaferrite powders synthesized by mechanochemical synthesis and heat-treated at $950^\circ C$ for 1 hour under an open atmosphere. The XRD patterns revealed that the primary phase in all powders was identified as the $SrFe_{12}O_{19}$ phase with a

hexagonal magnetoplumbite structure. The SEM image showed that the particles had a round morphology with partial agglomeration due to the reduction in particle size.

The magnetic properties, such as coercivity (H_c), magnetic flux density (B_s), residual magnetic flux density (B_r), and maximum energy product ($(BH)_{max}$) of the synthesized powders were found to be affected by the Sr/Fe ratio. The $(BH)_{max}$ values increased from 0.35 MGOe for the sample with a Sr/Fe ratio of 1:11 to 3.11 MGOe for the sample with a Sr/Fe ratio of 1:12.0. The presence of secondary phases such as α - Fe_2O_3 and SrO weakened the magnetic properties, as evidenced by the kink formation in the hysteresis loops. The weight fraction of the SrO phase was found to increase with a decrease in stoichiometry from 1:12 to 1:11, which correlated with the weakening of the magnetic properties.

In summary, the optimization of the Sr/Fe ratio can lead to the development of high-performance magnetic materials with improved magnetic properties. These findings can be useful for the design and synthesis of strontium hexaferrite powders for various industrial applications, such as in magnetic data storage devices, microwave devices, and sensors.

Acknowledgments

The authors gratefully acknowledge the financial support provided by the Scientific and Technological Research Council of Turkey (TUBITAK) under Grant Nos. 119M111 and 2210455, as well as the Department of Scientific Research Project of Karadeniz Technical University under Grant Nos. FDK-2018-7685, FYL-2018-7227, and FBA-2019-8162.

Author contributions

Sümran Bilgin: Conceptualization, Data curation, Investigation, Methodology
Sultan Öztürk: Project administration; Resources; Supervision

Kürşat İçin: Validation; Visualization; Roles/Writing-original draft; Writing - review & editing

References

- Zhivulin, V.E., et al., Effect of configurational entropy on phase formation, structure, and magnetic properties of deeply substituted strontium hexaferrites, *Ceramics International*, **2023**, 49(1):1069-1084
- İçin, K., et al., Investigation of nano-crystalline strontium hexaferrite magnet powder from mill scale waste by the mechanochemical synthesis: Effect of the annealing temperature, *Materials Chemistry and Physics*, **2022**, 290: 126513
- Darwish, M.A., et al., Heterovalent substituted $BaFe_{12-x}Sn_xO_{19}$ ($0.1 \leq x \leq 1.2$) M-type hexaferrite: Chemical composition, phase separation, magnetic properties and electrodynamic features. *Journal of Alloys and Compounds*, **2022**, 896:163117
- Akhter, T., et al., Optimization of structural, electrical, and magnetic properties of ytterbium substituted W-type hexaferrite for multi-layer chip inductors, *Ceramics International*, **2022**, 48(22):33177-33184
- Liu, R., et al., Magnetocrystalline anisotropy study of Co-substituted M-type strontium hexaferrite single crystals, *Ceramics International*, **2023**, 49(2):1888-1895
- Garehbaghi, S., and Kianvash, A., Effect of various parameters on the microstructure and magnetic properties of sintered Sr-hexaferrite, *Results in Physics*, **2019**, 12: 1559-1568
- Trusov, L.A., et al. Glass-Ceramic Synthesis of Cr-Substituted Strontium Hexaferrite Nanoparticles with Enhanced Coercivity, *Nanomaterials*, **2021**, 11
- Marjehal, M.A., Sedghi, A., and Baghshahi, S., Synergic effect of additives on the structure and properties of nano strontium hexaferrite synthesized via the gel combustion method, *Materials Science and Engineering: B*, **2022**, 278: 115631
- Stingaciu, M., et al., High magnetic coercive field in Ca-Al-Cr substituted strontium hexaferrite. *Journal of Alloys and Compounds*, **2021**, 883: 160768
- Kumar, A., et al., Lattice strain mediated structural and magnetic properties enhancement of strontium hexaferrite nanomaterials through controlled annealing. *Physica B: Condensed Matter*, **2021**, 600: 412592
- Shoubak, W.M., et al., Controlling the physical properties of polyacrylonitrile by strontium hexaferrite nanoparticles, *Polymer Bulletin*, **2023**
- Kim, C.S., and Yoon, S., Magnetic characterization of La^{3+} and Li^{1+} co-substituted M-type strontium hexaferrite, *Aip Advances*, **2023**, 13(2)
- Elanthamilan, E., et al., Strontium hexaferrite microspheres: Synthesis, characterization and visible-light-driven photocatalytic activity towards the degradation of methylene blue dye, *Optical Materials*, **2023**, 137
- Thakur, S., Raina, B., and Bamzai, K.K., Investigations on structural, spectroscopic and magnetic properties of yttrium barium orthoferrite and nickel doped strontium hexaferrite composites, *Applied Physics a-Materials Science & Processing*, **2022**, 128(4)
- Shaterian, M., Mohammadi-Ganjgah, A., and Balaei, M., Synthesis of potential nanostructures based on strontium hexaferrite for electrochemical hydrogen storage, *International Journal of Hydrogen Energy*, **2022**, 47(8): 5372-5379
- Mohammed, I., Mohammed, J., and Srivastava, A.K., Study of structural, morphological, optical bandgap and Urbach's tail of Ni^{2+} substituted Co_2Y -type strontium hexaferrite. *Materials Today-Proceedings*, **2022**, 62: 6634-6640
- Garcia-Martin, E., et al., Dense strontium hexaferrite-based permanent magnet composites assisted by cold sintering process. *Journal of Alloys and Compounds*, **2022**, 917
- Tiwary, R., Narayan, S., and Pandey, O., Preparation of strontium hexaferrite magnets from celestite and blue dust by mechanochemical route. *J Journal of Mining Metallurgy, Section B: Metallurgy*, **2008**, 44(1): 91-100
- Mordina, B., et al., Impact of graphene oxide on the magnetorheological behaviour of $BaFe_{12}O_{19}$ nanoparticles filled polyacrylamide hydrogel, **2016**, 97: 258-272
- Palomino, R.L., et al., Sonochemical assisted synthesis of $SrFe_{12}O_{19}$ nanoparticles, *Ultrason Sonochem*, **2016**, 29: 470-5
- Luo, J., Preparation of strontium ferrite powders by mechanochemical process, in *Applied Mechanics and Materials*. **2012**, 1736-1740

RESEARCH ARTICLE

Investigation of microstructure and wear performance of the high manganese steels

Ibrahim Arslan¹ , Mustafa Guven Gok^{*2}  and Halil Ibrahim Kurt³ ¹Arslankaya Casting Machine Industry and Trade and Joint-Stock Company, Gaziantep, Türkiye²Department of Metallurgical and Materials Engineering, Engineering Faculty, Gaziantep University, Gaziantep, Türkiye³Department of Aerospace Engineering, Faculty of Aeronautics and Astronautics Engineering, Samsun University, Samsun, Türkiye

Article Info

Article history:

Received: 29.04.2023

Revised: 23.05.2023

Accepted: 24.05.2023

Published Online: 08.06.2023

Keywords:

Hadfield steel

High manganese steel

Al5Ti1B

Wear

Microstructure

Abstract

High manganese steel is a metallic material that has a very important commercial value especially in heavy industry and stands out with its features such as high wear resistance, and deformation hardening. In order to further improve the properties of these steels, many studies have reported on adding various elements to their structures. However, there is still a lack of understanding of the relationship between the wear mechanism and strain hardening due to changes in the microstructure of high manganese steel during the wear process and the complex carbides it contains. In this study, Al5Ti1B (1% wt.), which is also used as a grain refiner in the metallurgy industry, was added. After melting, casting, and other production processes, test samples were prepared for microstructure analysis, hardness, and wear tests. It was observed that there were carbide phases at the grain boundaries of the test sample, and the hardness value was determined to be $254 \text{ HV} \pm 14$. The friction coefficients at 5 and 10 N loads increased by approximately 17.9% and 9.8%, respectively, by increasing the 500 m sliding distance to 1000 m. The effects of strain hardening and brittleness were also observed in the microstructure examinations after the wear test. In addition, a decrease in weight loss was observed, indicating that some deformation hardening occurred in the specimen during wear.

1. Introduction

Steels containing 1-1.4% carbon and 10-14% manganese in industrial applications and whose structure can remain 100% austenitic under suitable cooling conditions are called austenitic manganese steel or high manganese steel. These steels were first produced and patented in England in 1883 by Sir Robert Hadfield. For this reason, austenitic or high manganese steels are also known as Hadfield steel [1, 2]. High manganese steels have an excellent combination of hardness and ductility. This allows them to have high strength, toughness and wear resistance properties. The main reasons for choosing austenitic manganese steels for any particular application are, in order of importance: high toughness and wear resistance. Thanks to these properties, austenitic manganese steels are indispensable metallic materials for industrial areas such as excavation, railways, mining, petroleum and cement. They are used in the production of many other parts, such as crusher jaws, track shoes and rope pulleys, in these industrial areas [3-7].

The initial wear of cast parts subjected to wear under high loads not only shortens the service life of the parts but also significantly increases the production and repair costs of machine platforms. Such special parts should be selected from wear-resistant materials. Because the environmental conditions where abrasive wear is effective and the material properties that can be used in environments where impact wear is dominant are different from each other. However, it is very difficult to produce a uniform material that is resistant to all kinds of wear conditions in foundry conditions. For this reason, martensitic, pearlitic, austenitic and high-chromium steels are generally used in the mining industry, where wear is high, in oil drilling rigs, rolling mills, and excavation machines. Wear is not only a property of the material itself but also a property of the

engineering system. For this reason, it is both difficult and uneconomical to produce a material that will show high wear resistance in every working system. The best solution to this problem is the selection of materials suitable for working conditions, the optimization of hardness and microstructure. Important criteria affecting wear resistance of steels have been put forward by scientists as a result of experimental studies. When these studies are examined, it is understood that the hardness and microstructure of the material are the leading criteria that positively affect the wear resistance. The most effective way to control the hardness of steels is to change the carbon ratio and add the appropriate alloying elements [8-10]. In addition, according to the Hall-Petch equation, there is a relationship between grain size and mechanical properties in metallic materials. In the metallurgical industry, Al5Ti1B is recognized for its grain-refining effect [11].

In this study, Al5Ti1B was added to the high manganese steel alloy to improve its wear resistance. Then, the effect of the addition of Al5Ti1B on the hardness, microstructure and wear properties of the high manganese steel alloy systemically was investigated.

2. Materials and methods

First of all, a Y block wooden model was made to prepare the sand mold for casting. A mixture of fine grained 35-40 AFS (American Foundry Society) silica sand (SiO_2), resin (1.5% of sand) and hardener (25% of resin) was used in the preparation of molding sand. Then, high manganese steel GX120Mn13 alloy obtained from scrap and ores was melted by heating up to $1420 \text{ }^\circ\text{C}$ in an induction furnace (EGES-EGP1500SE) to obtain 15 kg of Y block samples for experimental studies. For this, after the weight of the molten metal in the furnace reached

Table 1. The chemical compositions of the materials used in experimental studies

| Material | % wt. | | | | | | | | | | |
|------------------|---------|---------|-------|-------|-------|------|---------|------|------|-------|---------|
| | C | Si | Mn | P | S | Cr | Fe | Ti | B | V | Al |
| GX120Mn13 | 1.1-1.3 | 0.3-0.5 | 12-14 | <0.1 | <0.04 | <1.5 | Balance | - | - | - | - |
| Al5Ti1B | - | 0.099 | - | - | - | - | 0.066 | 4.99 | 1.13 | 0.013 | Balance |
| Specimen | 1.29 | 0.637 | 13.5 | 0.056 | 0.004 | 1.68 | Balance | 0.03 | * | - | 0.3 |

* Since the atomic radius of the element boron is smaller than 1 Angstrom, it could not be detected by the current method.

1200 kg, the desired composition was tried to be achieved by adding the determined ores into the molten metal. In addition, when the temperature of the molten metal reached 1420 °C, perlite was added to the furnace to form slag on the molten metal surface. This slag formed on the liquid metal surface was removed and the melt was cleaned. After these processes, 15 kg of liquid metal were taken into the crucible and 1% by weight of Al5Ti1B was added. The chemical compositions of the materials used as a result of the spectral analysis (Oxford Instruments/Foundry-Master Xpert) are given in Table 1. For heat treatment, GX120Mn13 alloy samples with Al5Ti1B addition were placed in the annealing furnace and heated to 1050 °C for 5.5 hours, and kept at this temperature for 2.5 hours. Then the samples were taken from the annealing furnace and immersed in the water pool.

Afterwards, the samples were cut in the precision cutting device using a water coolant and hot-mounted in the mounting device (Metkon Ecopress52). Then, the hot-mounted samples were wet sanded in a rotating polishing machine (Bulupol Grinding/Polishing Machine) using SiC sandpapers of different grades between 600 mesh and 1200 mesh. In the final step, they were polished on a cloth using a 6-micron diamond solution. A Bursam-NDT brand/model hardness measuring device was used to determine the hardness of the polished samples. In this process, the average of at least 10 different hardness measurements was taken and the standard deviation value was

determined. On the other hand, the polished samples were etched in Nital (1-5 ml HNO₃ + 99-95 ml Ethyl Alcohol) solution for 10-20 seconds for microstructure studies. Optical microscopy (Nicon – Eclipse MA100) and scanning electron microscopy (SEM – ZEISS/GeminiSEM300) analyses were performed on the surfaces of GX120Mn13 samples having 1% by weight Al5Ti1B addition in this way. Moreover, the wear loss of the samples at 500 and 1000 m sliding distances under a load of 5-10 N was also investigated. The wear test was performed on the CSM Tribometer pin-on-disc wear device at a speed of 10 cm/sec. In order to determine the weight losses, the samples were weighed on a precision balance (Sartorius BL 210 S) before and after the wear test. Moreover, the scanning electron microscope was also used for the microstructure analysis of the worn surfaces of the samples after the wear test.

3. Results and Discussion

3.1. Microstructure and hardness evaluations

Microstructural images taken from the sample using optical and scanning electron microscopes are given in Figure 1 (a-d). In Figure 1 (a and b), microstructural images taken with an optical microscope at 5X and 50X magnification, respectively, were given. When these microstructures were examined, it was observed that the grains were homogeneously distributed and carbide phases were formed in the grain boundary regions as expected.

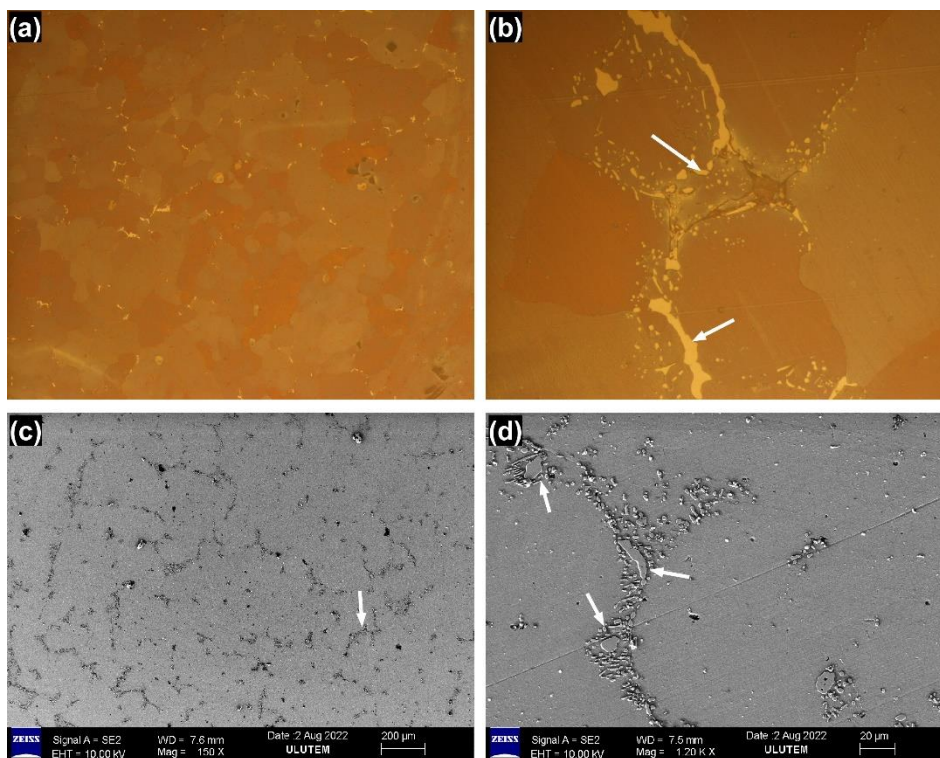


Figure 1. Images taken from the polished and etched sample surfaces by optical microscope ((a) - 5X) and ((b) - 50X) and scanning electron microscope ((c) - 150X) and ((d) - 1200X).

A similar situation was also evident in the microstructure images taken by SEM in Figure 1 (c and d). The carbide phase regions are indicated by arrows on the microstructure images. It is expected that the addition of Al5Ti1B to the chemical composition of high manganese steel decreases the austenite grain size and promotes the formation of carbides by reducing the amount of precipitate. In this case, the formation of carbide phases at the grain boundaries, will cause an increase in the hardness of the manganese steel. It is possible that small amounts of precipitated cementite are present at the grain boundaries of this high manganese steel. Tęcza and Klempka [12] also state that titanium-containing high manganese steel has secondary alloyed cementite at the grain boundaries and its amount is inversely proportional to the titanium content in the alloy.

When the graph of the hardness measurement result given in Figure 2 is examined, it is understood that the hardness of the steel with the Al5Ti1B addition was $254 \text{ HV} \pm 14$. In the literature [2], it is seen that the hardness value of high manganese steels is approximately 225 HV. Therefore, as a result of the addition of the Al5Ti1B to the high manganese steel, an increase in the hardness value occurred due to the formation of carbide phases. Especially since the carbides of the elements Ti and B in Al5Ti1B are characterized by their high hardness, the formation of these carbides significantly increased the hardness of the high manganese steel. These carbides were complex and precipitated at the austenite grain boundary regions and had important effects on the mechanical properties of the materials [13-15].

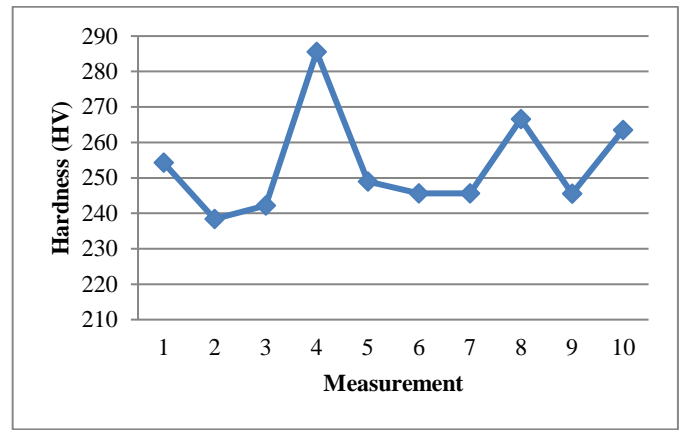


Figure 2. Hardness (HV) measurement results.

3.2. Wear Test Result

The wear coefficient and weight loss graphs obtained after 500 m and 1000 m of sliding distances at different loads (5N and 10N) as a result of the wear test are given in Figure 3 a-c, respectively. When the graphs were examined, it was seen that the friction coefficients increased rapidly from the beginning and reached a constant range after approximately 50 m of sliding distance. This increase was related to an increase in the contact area until full contact was made with the sample surface along the diameter of the pin. It was observed that the friction coefficients of the materials remained in a certain range as expected after a sliding distance of about 50 m. As seen in Figures 3 (a and b), this range was detected to be in a zigzag shape.

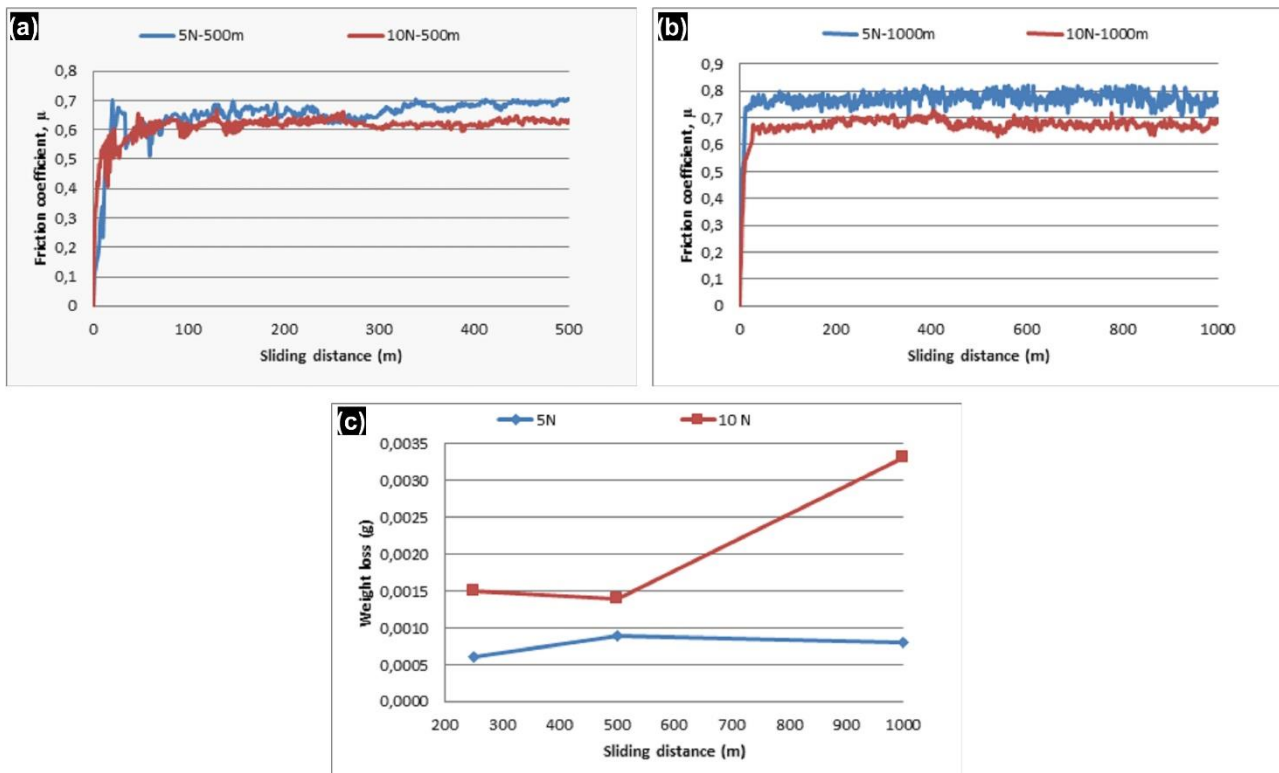


Figure 3. Friction coefficient-slip distance relationship ((a) 500m – 5N and 10N), ((b) 1000m – 5N and 10N) and weight loss-slip distance relationship (c).

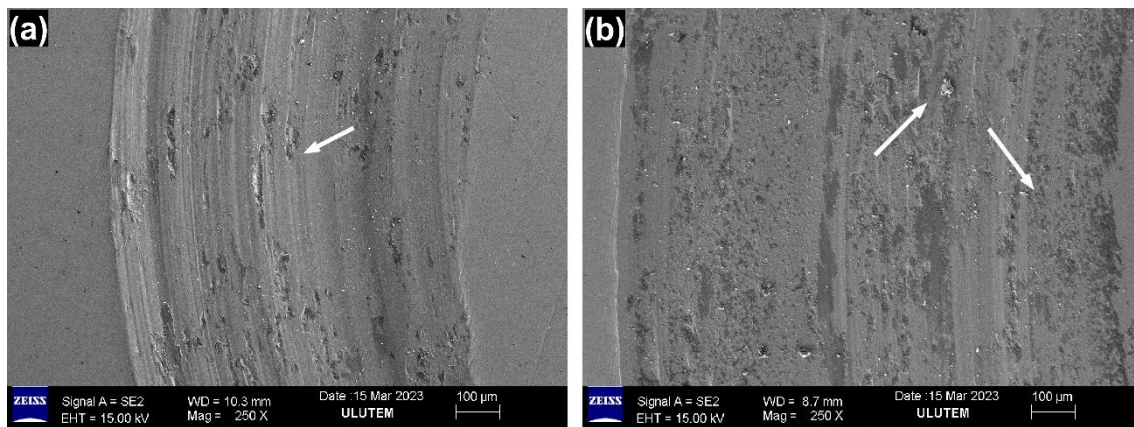


Figure 4. Wear surface images. (a) 5N load - 250m sliding distance and (b) 10N load - 1000m sliding distance.

While the average friction coefficient of the test specimen was 0.65 and 0.6139 μ at 500 m sliding distance and 5 - 10 N loads, respectively, these values increased to 0.7666 and 0.6739 μ with increasing the sliding distance to 1000 m. In addition, when the weight loss graph in Figure 3 (c) depending on the sliding distance at different loads was examined, it was understood that the weight loss increased with the increasing load (5 and 10 N). In the wear test, it was an expected result that with increasing load, the number of contact roughnesses increased and, consequently, the worn surface material increased. On the other hand, the amount of weight loss at 10 N load decreased up to 500 m and then increased. This indicated that strain hardening up to 500 m occurred in the high manganese steel sample, but then embrittlement occurred. In addition, the graph showed that the amount of weight loss in the sample at 5 N load first increased up to 500 m and then decreased. This proved that the 5 N load provided strain hardening of the sample only after 500 m sliding distance. It is well known that the additions of alloying elements and/or process parameters affect the hardness and wear characteristics of the materials and, in the literature, detailed studies were done which are in accord with our study [16-18].

3.3. Wear Surface Microstructure Investigation

In Figure 4 (a and b), SEM images of the wear surface of the samples were given after 5N load – 250 m slip distance and 10N load – 1000 m slip distance, respectively. The microstructures in Figure 4 show typical worn surface properties of high manganese steel. When the figures were compared, it was clearly understood that the amount of deformation on the wear surface increased with increasing load. It was clearly seen that there were tears and ruptures as a result of the wear test on the material surface (white arrows on the Figures). Due to the repeated plastic deformation with increasing load, the depth of surface scratches and surface cavities increases along with the amount. Brittle spalling and severe deformation are noticeable in some parts of the microstructure. Also, as expected, the wear occurred mostly in the matrix due to carbides (dark areas) formed at the grain boundaries. On the other hand, it was understood that the number of hard carbide phase regions on the surface increased with increasing deformation.

4. Conclusions

In this study, a test sample was produced by adding 1% by weight of Al5Ti1B to high manganese Hadfield steel. After the microstructure, hardness and wear tests, the following results were obtained.

1. A homogeneous grain structure was obtained, and carbide phases were observed in the grain boundary regions.
2. The hardness of the produced sample was 254 HV \pm 14. The fact that this hardness value is higher than the high manganese steel in the literature was attributed to the formation of complex carbides thanks to the addition of Al5Ti1B.
3. Average friction coefficients of 0.65 and 0.6139 μ were obtained at 500m sliding distance and 5 - 10 N loads, respectively. These values increased to 0.7666 and 0.6739 μ by increasing the slide distance to 1000 m. The effects of strain hardening and embrittlement were also observed.
4. Typical worn surface properties of high manganese steels were observed. Brittle fragmentation and severe deformation were noticeable in some parts of the microstructure. There were even micro-spallations and ruptures. It was understood that the wear occurred mostly in the matrix due to the carbides formed at the grain boundaries.

Acknowledgments

The authors thank to Gaziantep University Scientific Research Projects Unit for financially supporting this study with project number MF.YLT.22.02.

Author contributions

Ibrahim Arslan: Experimental studies; Casting and preparation of samples, Writing - original draft.

Mustafa Guven Gok: Investigation, Visualization, Microstructural Analyses, Writing - review & editing.

Halil Ibrahim Kurt: Project administration, Methodology, Wear test, Writing - review & editing.

References

1. Bhero, S., B., Nyembe, and K., Lentsoana, Common failures of Hadfield steel in application. in International Conference on Mining, Mineral Processing and Metallurgical Engineering (ICMMME) April. **2014**
2. Mahlami, C., and Pan, X., An Overview on high manganese steel casting. **2014**
3. Mahlami, C., and Pan, X., Challenges and developments of hadfield manganese steel castings based on service life. in Proceedings of the 71th World Foundry Congress, Bilbao, Spain. **2014**
4. Srivatsan, T.S., et al., Microstructure, tensile deformation and fracture behaviour of aluminium alloy 7055. *Journal of Materials Science*, **1997**, 32(11):2883-2894

5. Nam, N.D., Le Thi Chieu, N.M.T. and Khanh, P.M., Investigation of phase transformation mechanism of high manganese steel $Mn_{15}Cr_2$ heat-treated by subzero temperature process. *International Journal of Scientific and Engineering Research*, **2016**, 7(4):1527-1530
6. Bal, B., A study of different microstructural effects on the strain hardening behavior of Hadfield steel. *International Journal of Steel Structures*, **2018**,18:13-23
7. Luo, Q., and Zhu, J., Wear property and wear mechanisms of high-manganese austenitic Hadfield steel in dry reciprocal sliding. *Lubricants*, **2022**, 10(3):37
8. Benincá, F.P., et al., Evolution of morphology, microstructure and hardness of bodies and debris during sliding wear of carbon steels in a closed tribosystem. *Wear*, **2023**, 523:204809
9. Lee, S.H., et al., Effect of C-Mn ratio on the maximum hardness and toughness in TMCP steels with an identical carbon equivalent. *Journal of Materials Research and Technology*, **2020**, 9(4):8916-8928
10. Zhang, R., et al., The roles of Ce and Mn on solidification behaviors and mechanical properties of 7Mo super austenitic stainless steel. *Journal of Materials Research and Technology*, **2023**, 22:1238-1249
11. Arslan, İ., Gavgali, E., and Çolak, M., Kum Kalıba Dökülen Farklı Alüminyum Alaşımlarının Dökümünde Al5Ti1B ve Al10Sr İlavesinin Mikroyapı Özelliklere Etkisinin İncelenmesi. *Academic Platform-Journal of Engineering and Science*, **2019**, 7(2):237-244
12. Tęcza, G. and Garbacz-Klempka, A., Microstructure of cast high-manganese steel containing titanium. *Archives of Foundry Engineering*, **2016**, 16
13. Liu, D., et al., Effect of grain interior and grain boundary κ -carbides on the strain hardening behavior of medium-Mn lightweight steels. *Materials Science and Engineering: A*, **2023**, 871:144861
14. Zhou, Z., et al., Effect of nanoscale V2C precipitates on the three-body abrasive wear behavior of high-Mn austenitic steel. *Wear*, **2019**, 436-437:203009
15. Zhenming, X., et al., TiC as heterogeneous nuclei of the (Fe, Mn)3C and austenite intergrowth eutectic in austenite steel matrix wear resistant composite. *Materials Research Bulletin*, **2004**, 39(3):457-463
16. Yan, X., et al., Macroscopic and nanoscale investigation of the enhanced wear properties of medium-Mn steel processed via room-temperature quenching and partitioning. *Wear*, **2023**, 522:204711
17. Tang, Y. and Li, D.Y., Influences of C, Si and Mn on the wear resistance of coiled tubing steel. *Wear*, **2023**, 524-525:204854
18. Harsha, B.P., et al., Hardening behaviour, mechanical properties and wear evaluation of TRIP/TWIP manganese steels: A comprehensive review. *Materials Today: Proceedings*, **2023**

RESEARCH ARTICLE

An approach on determining micro-strain and crystallite size values of thermal spray barrier coated Inconel 601 super alloy

Nida Nur Erdoğan^{*1}, Aziz Barış Başıyigit²¹Kırıkkale University, Institute of Science, Department of Mechanical Engineering, Kırıkkale, Türkiye²Kırıkkale University, Faculty of Engineering and Architecture, Department of Metallurgical and Material Engineering, Kırıkkale, Türkiye

Article Info

Article history:

Received: 05.06.2023

Revised: 21.06.2023

Accepted: 30.06.2023

Published Online: 30.06.2023

Keywords:

Thermal barrier coatings

Inconel 601 alloy

Micro-strain analyze

Crystallite size

Abstract

Iron-based, nickel-based, and cobalt-based superalloys are the three types of superalloys utilized in high-temperature applications. Inconel 601 is a nickel-based superalloy that's used especially in aerospace, heat treatment, and gas turbine engine applications. In this study, thermal barrier coating (TBC) was applied approximately at 100, 200 and 300 μm ceramic top coating thicknesses and X-Ray Diffraction (XRD) analyzes were performed. NiCrAlY metallic powder was used for bond coating and 8% YSZ ceramic powder was used for ceramic top coating. Crystallite sizes and micro-strain values were calculated with the Scherrer Equation, Williamson-Hall method and Modified Scherrer (Monshi-Scherrer) equation of the compounds obtained at the peak points in XRD analysis.

1. Introduction

Super-alloys are used in high-temperature applications because of their satisfactory mechanical strength, stability, and resistance to wear and corrosion. They are classified into three major classes based on their nickel, iron, and cobalt content [1]. Nickel-based super-alloys can be efficiently produced by alloying with elements such as chromium, and/or aluminum in a face centered cubic nickel matrix [2]. Nickel-based super-alloys have a nickel content of 30-75% and a chromium content of up to 30% by weight. Furthermore, some alloying elements such as titanium, cobalt, boron, zirconium, and carbon are also added to their compositions [3]. In applications where very high temperatures are present, such as jet engines, aviation vehicle parts, and industrial heaters, Inconel 601 alloy is also preferred. The face-centered cubic (FCC) gamma phase, carbides and borides, delta and sigma phases, and other topologically close-packed structures in the microstructure of super-alloys increase the alloy's strength and provide resistance to corrosion and oxidation [4,5].

Whether the mechanical properties, wear and corrosion resistance of super alloys is insufficient, the requisite properties can be achieved by subjecting these materials to heat treatment and coating methods. It is anticipated that when service life is enhanced and performance standards rise, there will be more usage fields for super alloys. Diffusion and overlay coating, thermal barrier coating are the three types of surface hardening techniques used on super-alloys. While diffusion coating and overlay coating methods are primarily used to protect materials from abrasion, oxidation, and corrosion, thermal barrier coating processes are used to shield materials from high ranges of heat [4].

Stress relief annealing, full annealing, diffusion coating and age hardening are the four heat treatments that are most frequently used on super-alloys [6,7]. By preventing creep, thermal barrier coatings (TBC) are used to lower oxidation rates and heat flow in materials. These systems are mostly used in

aircrafts and gas turbines. TBCs are made up of a bond coat, a thermally generated oxide (TGO), and a ceramic top coat [8,9].

Crystallite size is frequently determined in monodisperse microstructures using X-ray diffraction patterns and other experimental approaches such as transmission electron microscopy. Dislocations are prevented from moving freely throughout a material by grain boundaries. The stress field of the grain boundary defect zone, which is typically aligned along the boundaries, prevents dislocation from propagating. Therefore, one popular method of boosting strength is to reduce the grain size. The Hall-Petch connection provides the size-force relationship for crystallites. Grain boundaries are the favored locations for the beginning of corrosion and the precipitation of new phases from solids due to their high interfacial energy and relatively weak bonding [10-11].

Studies for various substrate materials and coatings are also intriguing, even though there are no studies for superalloys in the literature. Mateus D.F.A. et. al., throughout the thickness of the titanium nitride thin films, the crystallite size and micro-strain were examined. For two different thicknesses, the films were deposited onto 316 stainless steel substrates using the Plasma Assisted Physical Vapor Deposition process (PAPVD). The crystallite size and microstrain as a function of film depth were examined for the (111) and (200) orientations. Both films exhibit anisotropic behavior, according to the results [12]. Augustin A. et.al., discovered that the crystallite size in electrodeposited copper plating fluctuates with deposition current density, and they evaluated the crystallite size and micro-strain in the plating using the Williamson-Hall method. The values of crystallite sizes obtained from TEM micrographs were found to be consistent with those obtained from the Williamson-Hall method. The existence of nano-twins in the coating also contributed to the copper coating's micro-strains [13]. Pilliadugula R. et.al., The XRD pattern of beta-Ga₂O₃ powder, synthesized at low temperature using a template-free two-step hydrothermal process, is fully examined using several methods

of analysis. The crystallite sizes as well as the micro-strains of the micro-structures are studied and compared. For the inquiry, in addition to the classic Scherrer's formula (S-average, LF, and LFTZ), the modified Williamson-Hall (W-H) approach with UDM, USDM, and UDEDM, and the Size-Strain Plot (SSP) method were used. It was discovered that the crystallite sizes generated from the UDM modified W-H analysis and SSP models closely matched the crystallite sizes observed in the TEM micrograph [14].

In this study, Thermal barrier coating method was applied on Inconel 601 samples approximately at 100, 200 and 300 μm ceramic top coating thicknesses and XRD analyzes were performed. Crystallite sizes and microstrain values of 100, 200, 300 μm 8% YSZ TBC coated Inconel 601 samples were calculated by Scherrer, Monshi Scherrer and Williamson-Hall methods. Scherrer equation is a formula in XRD and X-Ray Crystallography that relates the size of submicron crystallites in a solid to the broadening of a peak in the diffraction pattern. The Williamson-Hall analysis is that the expansion is functions of the peak width if it is both size-induced and strain-induced.

2. Materials and methods

The Inconel 601 experimental material used in the study is constructed of circular bars measuring 16 mm in diameter by 400 mm in length that have been lightly cold rolled to obtain a clean finish. Wire erosion was used to cut this material to prepare 4 samples per each case depth in dimensions of $\text{Ø}16 \times 7$ mm.

The chemical composition of the Inconel 601 raw material in the study was determined using an argon optical spectrometer of the AmateX brand and Spectromaxx model. The Inconel 601 alloy's average chemical composition was obtained and is shown in Table 1.

Table 1. The chemical composition of Inconel 601

| Element | Chemical composition (%wt) |
|---------|----------------------------|
| Ni | 58,225 |
| Cr | 23,000 |
| Fe | 16,375 |
| Al | 1,000 |
| C | 0,100 |
| Mn | 0,320 |
| Si | 0,430 |
| Cu | 0,034 |
| Others | 0,516 |

For thermal barrier coating process, initially, samples were cleaned using sandblasting. The samples were then put inside the coating device. On the Inconel 601 experimental material, NiCrAlY powder was applied as the bond coat material using the HVOF spray method, and 8% YSZ was coated as the ceramic top coat material over the bond coat using the APS method.

The scanning angle range used for XRD (X-Ray Diffraction) analysis was $10\text{-}90^\circ$, and the scanning speed was set to 2 deg/min. A Rigaku Ultima IV X-ray diffractometer with a copper-targeted X-ray tube and operating voltage and current settings of 40 kV and 30 mA was used for the analysis.

3. Results and discussion

Sample 1 represents 100 μm , sample 2 represents 200 μm , sample 3 represents 300 μm ceramic top coated samples and sample 4 represents Inconel 601 raw material. Fig.1. shows the XRD datas of sample 1, sample 2, sample 3 and sample 4. The

letter t represents the tetragonal structure and the letter c represents the cubic structure. The lattice parameters and crystal systems given in the Table.2 were found through the X-Pert Highscore Plus software.

Table 2. Lattice parameters and crystal systems of compounds obtained from XRD datas

| Compounds | Lattice parameters | | | Crystal Systems |
|--|--------------------|--------------------|--------------------|-----------------|
| | a (\AA) | b (\AA) | c (\AA) | |
| $\text{Y}_{0.19}\text{Zr}_{1.81}\text{O}_{3.9}$ | 3,616 | 3,616 | 5,158 | t |
| $\text{O}_{3.87}\text{Zr}_{1.74}\text{Y}_{0.26}$ | 3,625 | 3,625 | 5,14 | t |
| ZrO_2 | 5,129 | 5,129 | 5,129 | c |
| $\text{Ni}_{2.88}\text{W}_{0.32}\text{Cr}_{0.8}$ | 3,573 | 3,573 | 3,573 | c |
| Ni_4 | 3,571 | 3,571 | 3,571 | c |
| CrNi | 3,591 | 3,591 | 3,591 | c |
| Fe_4 | 3,49 | 3,49 | 3,49 | c |

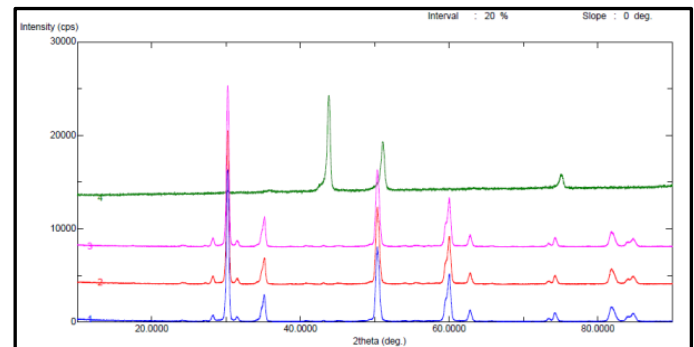


Figure 1. XRD data of Sample 1, Sample 2, Sample 3 and Sample 4

- Analyzing the XRD results of Sample 1's, at 30.2° , 35.2° , 50.3° , 62.8° , 74.2° , 81.8° , and 84.7° from the (101), (110), (112), (211), (202), (220), (213) and (310) planes of $\text{Y}_{0.19}\text{Zr}_{1.81}\text{O}_{3.9}$ in tetragonal structure,
- Analyzing the XRD results of Sample 2's, at 30.2° , 35° , 50.3° , 59.8° , 62.7° , 73.9° , 81.8° and 84.5° from the (101), (110), (112), (211), (202), (220), (213) and (310) planes of $\text{O}_{3.87}\text{Zr}_{1.74}\text{Y}_{0.26}$ in tetragonal structure and from the (111), (020), (022), (131), (222), (040), (133), (042) planes of ZrO_2 in cubic structure,
- Analyzing the XRD results of Sample 3's, at 30.2° , 35.1° , 50.2° , 59.9° , 62.7° , 74.1° , 81.7° and 84.7° from the (101), (110), (112), (211), (202), (220), (213) and (310) planes of $\text{Y}_{0.19}\text{Zr}_{1.81}\text{O}_{3.90}$ in tetragonal structure and from the (111), (020), (022), (131), (222), (040), (133), (042) planes of ZrO_2 in cubic structure,
- Analyzing the XRD results of Sample 4's, at 43.9° , 51.1° and 75.2° from the (111), (200) ve (220) planes of $\text{Ni}_{2.88}\text{W}_{0.32}\text{Cr}_{0.8}$, Ni_4 , CrNi and Fe_4

diffraction was recorded. Studies that are similar to this one [15–17] support these findings.

Above 2370°C , zirconia is cubic, tetragonal between 2370°C and 1170°C , and monoclinic below 1170°C [18]. Cubic ZrO_2 diffraction is clearly observed in samples with ceramic top coating thicknesses of 200 and 300 μm . The cooling of the

samples at room temperature following the process, which varies depending on the TBC processing temperature and coating thickness is expected to have an effect on the visual cubic structure of the zirconia.

The raw Inconel 601 sample (Sample 4) had CrNi and Ni_{2.88}W_{0.32}Cr_{0.8} diffractions, as well as cubic Ni₄ and Fe₄ structures, as predicted. The Ni matrix, clearly generate bonds with the alloying elements W and Cr.

3.1. Calculation of Crystallite Sizes, Strain Density and Micro-Strain Values with Scherrer Equation

Scherrer equation is a formula in XRD and X-Ray Crystallography that relates the size of submicron crystallites in a solid to the broadening of a peak in the diffraction pattern.

The Scherrer equation, used in both X-ray crystallography and X-ray diffractometry, relates the size of submicron crystallites in Equation (1), where D is the nanocrystal size, K is the shape factor, typically taken to be 0.89 for ceramic materials is the wavelength of radiation in nanometers, is the diffracted angle of the peak, and is the full width at half maximum of the peak in radians [19,20].

$$D = \frac{K\lambda}{\beta \cdot \cos\theta} \tag{1}$$

Crystallite sizes calculated using the Scherrer equation Table.3 has been given.

Table 3. Crystallite sizes

| Peak No | Sample 1 | Sample 2 | Sample 3 | Sample 4 |
|---------|------------------------|----------|----------|----------|
| | Crystallite sizes (nm) | | | |
| 1 | 21,3 | 21,3 | 21,3 | 22,2 |
| 2 | 27,1 | 27,2 | 31,1 | 17,5 |
| 3 | 18,9 | 14,1 | 20,7 | 18,5 |
| 4 | 26,5 | 23,8 | 26,5 | - |
| 5 | 17,1 | 17,1 | 20,1 | - |
| 6 | 21,5 | 21,5 | 21,5 | - |
| 7 | 11,2 | 16,9 | 11,2 | - |
| 8 | 17,3 | 17,3 | 15,4 | - |

When the crystallite sizes calculated from XRD peak points with Scherrer's equation are examined, the mean crystallite size for Sample 1 is 20.1 nm, the mean crystallite size for sample 2 is 19.9 nm, the mean crystallite size for sample 3 is 20.98, and the mean crystal size for sample 4 is 19.4 nm. The formulas and explanations of D, δ and ε are given below.

D = crystallite size,

$$\delta = \delta = \frac{1}{D^2} \text{ strain density,} \tag{2}$$

$$\epsilon = \frac{\beta}{4 \tan \theta} \text{ microstrain [17,18].} \tag{3}$$

When δ and ε values are calculated for the major peak points of the samples,

- For Sample 1, δ = 2.204 x 10⁻³ nm⁻², ε = 6 x 10⁻³,
- For Sample 2, δ = 2.204 x 10⁻³ nm⁻², ε = 5.9 x 10⁻³,
- For Sample 3 δ = 2.204 x 10⁻³ nm⁻², ε = 5.92 x 10⁻³,

- For Sample 4, δ = 2.03 x 10⁻³ nm⁻², ε = 4.67 x 10⁻³ are found.

3.2. Calculation of Micro-Strain Values by Williamson-Hall (UDM) Method

The Williamson-Hall method, on the other hand, assumes that the broadening of the peaks is the cumulative effect of size-induced expansion and strain-induced expansion. William-Hall method; It can be expressed as β_{total} = β_{size} + β_{strain}. Uniform deformation model (UDM), also known as the modified W-H method;

$$\epsilon = \frac{\beta}{4 \cdot \tan \theta} = \beta_{\text{strain}} \cdot \frac{\cos \theta}{4 \cdot \sin \theta} \tag{4}$$

$$\beta_{\text{total}} = \beta_{\text{size}} + \beta_{\text{strain}} = \frac{K\lambda}{D \cdot \cos \theta} + 4\epsilon \frac{\sin \theta}{\cos \theta} \tag{5}$$

$$\beta_{\text{total}} \cdot \cos \theta = \frac{K\lambda}{D} + 4\epsilon \sin \theta \tag{6}$$

can be expressed [20]. According to the Williamson-Hall (UDM) method, the equation expressed in Equation specifies a line whose slope is ε and the point where it intersects the y-axis is $\frac{K\lambda}{D}$. Figure 2 shows Williamson Hall (UDM) plots with the peak values of the samples.

The slope of the Williamson-Hall plots plotted with the values of the peak points of the samples, hence the total microstrain values from the size and deformation of the samples, are 0,39x10⁻³, 0,13x10⁻³, 0,29x10⁻⁴ and -0,26x10⁻³ respectively. It is positive values indicate that microstrain is under the influence of tensile stress, while negative values indicate that it is under the influence of compressive stress.

3.3. Calculation of Crystallite Sizes with Modified Scherrer (Monshi – Scherrer) Equation

The premise of the modified Scherrer formula is that, by applying the least squares approach to mathematically reduce the source of mistakes, reduce errors and obtain the average value of L via all peaks. The Monshi-Scherrer equation is expressed below. Taking the logarithm of both sides of the Scherrer equation;

$$\ln \beta = \ln \frac{K\lambda}{D \cdot \cos \theta} = \ln \frac{K\lambda}{D} + \ln \frac{1}{\cos \theta} \tag{7}$$

A straight line with an intercept of around lnK/L and a slope of about one must be obtained if the results of ln versus ln(1/cosθ) are plotted. Since tan45° = 1, this line should theoretically have a slope of 45°. The least squares method, however, provides the best slope and most accurate lnK/L because mistakes are linked to experimental data [21].

The intercept is first obtained, and then the exponential of the intercept is found as;

$$e^{\text{intercept}} = \frac{K\lambda}{D} \tag{8}$$

Figure 3 shows Monschi-Scherrer plots plotted with the peak values of the samples.

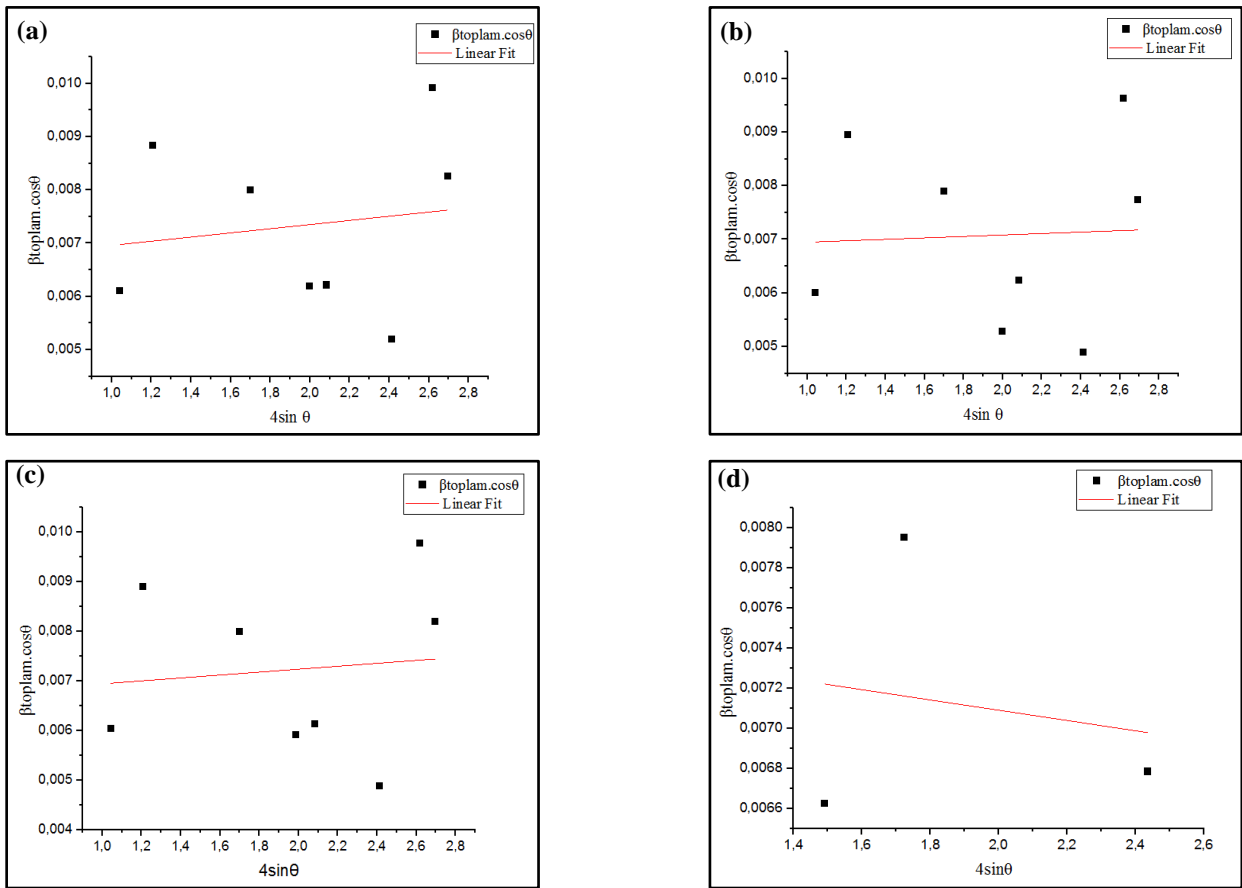


Figure 2. Williamson Hall (UDM) plots plotted with the peak values of the samples. (a) Sample 1 (b) Sample 2 (c) Sample 3 (d) Sample 4

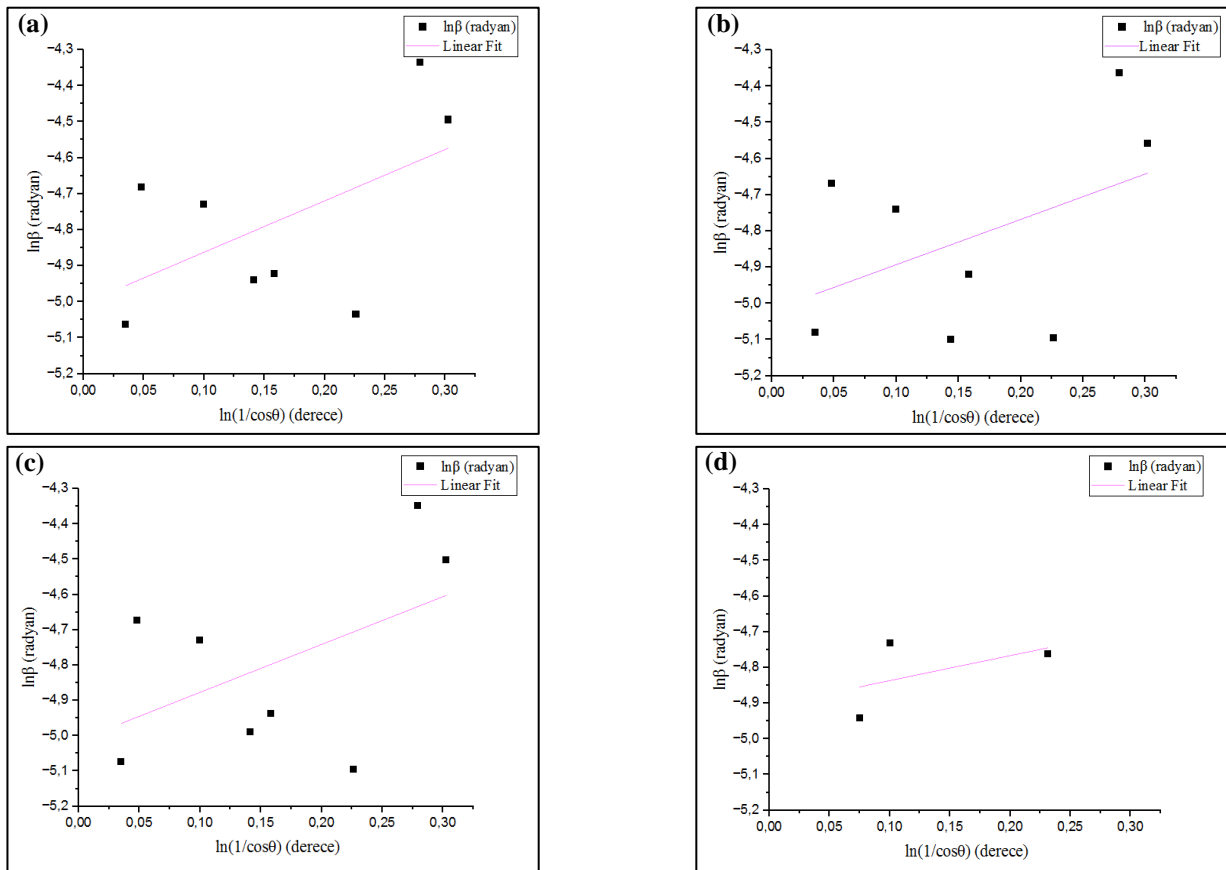


Figure 3. Monchi-Scherrer plots plotted with the peak values of the samples. (a) Sample 1 (b) Sample 2 (c) Sample 3 (d) Sample 4

It is seen that the points where the Monschi-Scherrer graph drawn for Sample 1, Sample 2, Sample 3 and Sample 4 intersect the y-axis are -5,00515, -5,01819, -5,01257 and -4,90664, respectively.

When the $e^{\text{intercept}} = \frac{K\lambda}{D}$ equations are met, the crystallite sizes of the samples found by the Monschi-Scherrer equation are 21,6, 21,9, 24,4 and 19,6 nm, respectively.

4. Conclusions

As a result, crystallite sizes and micro-strain values of coatings and raw Inconel 601 super-alloy were calculated by XRD patterns applied to 100, 200 and 300 micron TBC coated with 8% YSZ powder on experimental material Inconel 601. Accordingly, the crystallite sizes obtained by Scherrer's equation were calculated as 20,1 nm, 19,9 nm, 20,98 nm, 19,4 nm for 100,200,300 μm ceramic top-coated and Inconel 601 samples, respectively. The crystallite sizes obtained by the modified Monshi-Scherrer equation are 21,6, 21,9, 24,4 and 19,6 nm, respectively. The microstrain values obtained by Williamson-Hall method are; $0,39 \times 10^{-3}$, $0,13 \times 10^{-3}$, $0,29 \times 10^{-4}$ and $-0,26 \times 10^{-3}$ respectively. This is because Williamson-Hall analysis, both size-induced and strain-induced Scherrer equation are functions of the peak width of the size-induced expansion only. However, the results obtained by these two distinct methods are highly correlated and will show the same trends as the synthesis conditions change. Although the Williamson-Hall method makes a lot of assumptions, it can be useful when applied in a relative sense. For instance, a study of numerous powder patterns of the same chemical compound synthesized under various conditions may reveal trends in crystallite size and strain. Based on the results, material strength will be stronger with lower particle sizes computed using the Scherrer equation, and hence smaller grain size. Nonetheless, the experiment can be repeated and the findings compared for various superalloy compositions and coatings.

Acknowledgments

Authors would like to thank Kırıkkale University Scientific Research Projects Department for financial supports (Project Code: 2022/053).

Author contributions

N. N. Erdoğan: Conceptualization, Data curation, Formal analysis, Funding acquisition, Investigation, Resources, Software, Visualization, Roles/Writing - original draft, Review & editing

A.B.Başığit: Conceptualization, Data curation, Formal analysis, Funding acquisition, Investigation, Methodology, Project administration, Resources, Supervision, Validation, Roles/Writing - original draft, Review & editing

References

1. Çay, V.V., Ozan, S., Süperalaşımalar ve Uygulama Alanları, Doğu Anadolu Bölgesi Araştırmaları, **2005**, 3(2):178-188
2. Akça, E., Gürsel, A., A Review on Superalloys and IN718 Nickel-Based Inconel Superalloy, Periodicals of Engineering and Natural Sciences, **2015**, 3(1)
3. Atmaca, E.S., Inconel 718 Süperalaşımının PVD Yöntemi ile AlTiN ve CrN Kaplanması ve Karakterize Edilmesi, Gazi Üniversitesi, Metalurji ve Malzeme Anabilim Dalı, Yüksek Lisans Tezi, Nisan **2015**
4. Reed, R.C., The Superalloys Fundamentals and Applications, Cambridge University Press, **2006**, 1-28
5. Donachie, M.J., and Donachie, S.J., Superalloys A Technical Guide, Second Edition, ASM International, **2002**, 25-39
6. Watson, J.E., Superalloys, Production, Properties and Applications, Nova Science Publishers, Inc. New York, **2011**, 25-44
7. Heubner, U., Nickel Alloys, CRC Press Taylor & Francis Group, Germany, **2018**, 129-160
8. ASM Specialty Handbook: Nickel, Cobalt, and Their Alloys, **2000**, 9-54, 287
9. Galetz, M.C., Coatings on Superalloys, Superalloys, Coatings for Superalloys, InTech, **2015**
10. Doherty, R.D., Hughes, D.A., Humphreys, F.J., Jonas, J.J., Jensen, D.J., Kassner, M.E., King, W.E., McNelley, T.R., McQueen, H.J., Rollett, A.D., Current issues in recrystallization: A review, Materials Science and Engineering: A. **1997**, 238(2):219-274
11. Allen, S., and Thomas, E., The Structure of Materials. New York: John Wiley & Sons, Inc. **1999**
12. Mateus, D., et. al., Crystallite Size and Micro-strain evolution in TiN Thin Films, Entre Ciencia E Ingenieria, WOS:000420316600007, **2011**, 9:94-106
13. Augustin, A., et. al., Crystallite Size Measurement and Micro-strain Analysis of Electrodeposited Copper Thin Film using Williamson-Hall Method, International Conference on Condensed Matter and Applied Physics, Proceedings Paper, **2016**, 1728
14. Pilliadugula, R., Gopalakrishnan, N., Crystallite size and micro-strain investigations of hydrothermally synthesized beta-Ga₂O₃ by different analytical methods, Functional Materials Letters, **2020**, 13(5)
15. Jamail, H., Razavi, R.S., Investigation of Thermal Shock Behavior of Plasma-Sprayed NiCoCrAlY/YSZ Thermal Barrier Coatings, Advanced Materials Research, **2012**, 472-475:246-250
16. Loghman-Estarki, M.R., Nejati, M., Edris, H., Razavi, R.S., Jamali, H., Pakseresht, A.H., Evaluation of hot corrosion behavior of plasma sprayed scandia and yttrium-stabilized nanostructured thermal barrier coatings in the presence of molten sulfate and vanadate salt, Journal of the European Ceramic Society 35, **2015**, 693-702
17. Sathish, S., Geetha, M., Aruna, S.T., Balaji, N., Rajam, K.S., Asokamani, R., Studies on plasma sprayed bi-layered ceramic coating on bio-medical Ti-13Nb-13Zr alloy, Ceramics International 37, **2011**, 1333-1339
18. Kırmalı, Ö., Özdemir, A.K., Zirkonya Esaslı Seramikler, İnönü University Sağlık Bilimleri Dergisi 2, **2012**, 15-18
19. Kolhe, M.L., Karande, K.J., Deshmukh, S.G., Artificial Intelligence, Internet of Things (IOT) and Smart Materials for Energy Applications, CRC Press, **2022**, 32
20. Rabiei, M., et.al., Comparing Methods for Calculating Nanocrystal Size of Natural Hydroxyapatite Using X-Ray Diffraction, Nanomaterials **2020**, 10, 1627
21. Monshi, A., Foroughi, M.R., Monshi, M.R., Modified Scherrer Equation to Estimate More Accurately Nano-Crystallite Size Using XRD. World J. Nano Sci. Eng. **2012**, 2:154-160

RESEARCH ARTICLE

Examining the relationship between mechanical impact intensity and the decomposition temperature of celestite

Kürşat İçin^{*1}, Sümran Bilgin¹, Sefa Emre Sünbül² and Sultan Öztürk¹

¹Karadeniz Technical University, Engineering Faculty, Metallurgical and Materials Engineering Department, Trabzon, Türkiye

²Gaziantep University, Engineering Faculty, Metallurgical and Materials Engineering Department, Gaziantep, Türkiye

Article Info

Article history:

Received: 19.04.2023

Revised: 21.06.2023

Accepted: 30.06.2023

Published Online: 30.06.2023

Keywords:

Celestite

Thermal decomposition

Mechanochemical synthesis

Abstract

The aim of this study was to investigate the impact of mechanochemical synthesis time on the decomposition of sulfated celestite ore and to understand the reactions, phases, and thermal transformations involved in the formation of strontium carbonate using various characterization techniques. The study found that the conversion rate of celestite ore to strontium carbonate increased with increasing mechanochemical synthesis duration, and that the peak intensities of SrCO₃ were highest at 100 minutes but decreased at 200 minutes, indicating that the crystal structure was disrupted beyond a certain duration. The transformation temperatures in DTA curves also decreased with increasing synthesis duration due to the increase in energy of the particles. Overall, this study provides valuable insights into the mechanistic aspects of strontium carbonate decomposition.

1. Introduction

Strontium carbonate is a widely used compound in various industries, including electronics, ceramics, and metallurgy [1]. Traditional methods of producing strontium carbonate involve high-temperature processes, which are energy-intensive and environmentally harmful. Recently, researchers have been exploring new methods of producing strontium carbonate using mechanochemical synthesis [2].

Mechanochemical synthesis is a process that involves the use of mechanical energy to drive chemical reactions [3]. It is a promising method for producing strontium carbonate due to its simplicity, low energy consumption, and high yield. In this process, strontium oxide and carbon dioxide are mechanically milled together in the presence of a suitable catalyst to produce strontium carbonate. One of the key advantages of mechanochemical synthesis is that it can be carried out at room temperature, which eliminates the need for high-temperature furnaces and reduces energy consumption [4-6]. The process also produces less waste and is more environmentally friendly than traditional methods. Another advantage of mechanochemical synthesis is that it allows for the production of strontium carbonate with controlled particle size and morphology. This is important for applications such as catalysis, where particle size and morphology can have a significant impact on performance [7-9]. Despite the many advantages of mechanochemical synthesis, there are still some challenges that need to be addressed. For example, the process can be sensitive to the presence of impurities and requires careful control of the milling conditions to ensure consistent results. Nevertheless, ongoing research in this area is expected to lead to further improvements in the process [10, 11]. In summary, mechanochemical synthesis is a promising method for producing strontium carbonate with low energy consumption, high yield, and controlled particle size and morphology. As research in this area continues, we can expect to see the

development of more efficient and effective methods for producing this important compound.

During mechanochemical synthesis, the mechanical energy generated by the milling process can induce structural changes in celestite, leading to the formation of intermediate phases and ultimately to the production of strontium carbonate. The milling process can also affect the size and morphology of the resulting particles, which can have important implications for the properties and performance of the final product [12, 13].

The extent and nature of the mechanical effects depend on several factors, including the type of milling equipment used, the milling time, and the milling intensity. These factors can be optimized to control the properties of the final product and to minimize the formation of unwanted byproducts [14]. Understanding the mechanical effects of mechanochemical synthesis is important for the development of efficient and effective methods for producing strontium carbonate. Further research is needed to elucidate the underlying mechanisms of the process and to optimize the milling conditions for the production of high-quality strontium carbonate [15, 16].

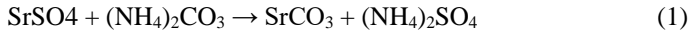
The aim of this study is to investigate the effects of mechanical activation on the transformation temperature of celestite during mechanochemical synthesis. The study will focus on the relationship between the mechanical intensity of the milling process and the transformation temperature of celestite to strontium carbonate.

2. Materials and methods

The celestite ore used in all experimental studies was obtained free of charge from Barit Maden Turk A.Ş. The chemical analysis of the celestite ore used in all experiments was determined by atomic absorption spectrometry (AAS) and presented in Table 1. As shown in the table, the structure of the celestite ore contains three different sulfate compounds: SrSO₄, CaSO₄, and BaSO₄. The concentrated celestite ore was found to

contain 95.5% by weight of strontium sulfate (SrSO_4) compound. In addition to SrSO_4 , calcium sulfate (CaSO_4) was also found in the ore, accounting for 3% by weight.

A mixture of strontium sulfate (SrSO_4) and ammonium carbonate ($(\text{NH}_4)_2\text{CO}_3$) was prepared according to Equation 1 for investigating the mechanochemical conversion of celestite ore to strontium carbonate.



A 1:1 stoichiometric ratio was used for SrSO_4 and $(\text{NH}_4)_2\text{CO}_3$, and the mechanochemical synthesis process was carried out for 10, 100, and 200 minutes using a 5 mm diameter WC ball, a 1:10 powder-to-ball ratio, and a constant rotation speed of 450 rpm. The experiment was conducted at the Department of Metallurgy and Materials Engineering in Karadeniz Technical University, using a Fritsch Premium Line 5 planetary ball mill.

The particle morphologies and energy dispersive X-ray (EDX) analysis of the resulting SrCO_3 powders were observed using a Zeiss EVO LS10 scanning electron microscope (SEM). Phase transformation temperatures of the SrCO_3 powders obtained were determined using a Linseis PT1600 DSC/DTA/TG device, with differential thermal analysis (DTA) and thermal gravimetric analysis (TGA) methods. The thermal analyses were conducted between 30-1200 °C at a heating rate of 30 °C/min.

Table 1. Composition of the celestite ore

| Compound | Weight percent (%) |
|-------------------------|--------------------|
| SrSO_4 | 95,5 |
| CaSO_4 | 3,0 |
| BaSO_4 | 0,5 |
| SiO_2 | 0,5 |
| Fe_2O_3 | 0,5 |

3. Results and discussion

In our study, concentrated celestite ore, obtained free of charge from Barit Maden Turk A.S., was used as the source of strontium carbonate. Scanning electron microscope (SEM) images of the concentrated celestite ore taken from different sieve ranges are presented in Figure 1. Upon examination of the SEM images, it was observed that the dominant particle shape of the powder was generally round and angular. Considering that using such widely distributed ore could result in an inhomogeneous particle size distribution in the production of SrCO_3 , celestite ore in the -1000/+125 μm sieve range was preferred in this study.

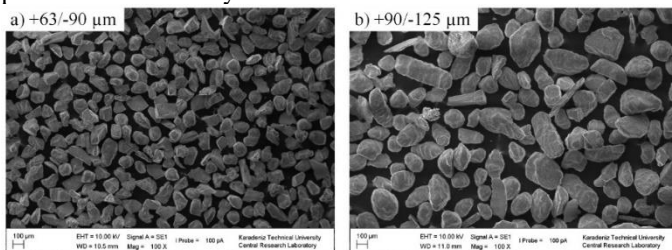


Figure 1. Scanning electron microscope (SEM) images of concentrated celestite ore obtained from different sieve intervals.

The study utilized differential thermal analysis (DTA) to investigate the temperature-induced phase transitions of celestite ore (Figure 2). The DTA curve of the ore exhibited three distinct endothermic peaks. The first peak corresponds to the thermal decomposition temperature range of CaCO_3 , which is present along with CaSO_4 in the ore's structure. This decomposition reaction starts at 670 °C and completes at 832 °C (peak 1). The second endothermic peak, which is of low intensity, represents the phase transition of SrCO_3 , another impurity present in the celestite ore. This transition is shown by peak 2, beginning at 835 °C and ending at 920 °C, where the α - SrCO_3 phase transforms to β - SrCO_3 phase. The third and most intense endothermic peak depicts the thermal decomposition of SrCO_3 in the ore. As per the thermal reaction associated with peak 3, it initiates at 1130 °C and completes at 1200 °C.

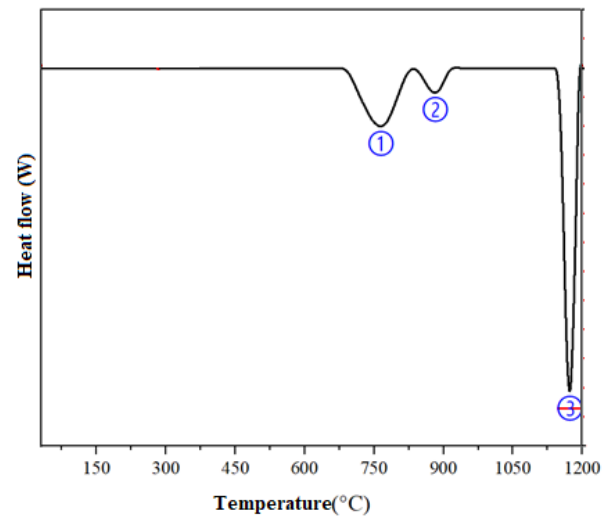


Figure 2. DTA analysis of domestic celestite ore

The SEM and EDS analysis results presented in Figure 3 provide important information regarding the progress of the mechanochemical synthesis process. The EDS analysis confirms that unreacted strontium sulfate is still present in the powder mixture after 10 minutes of synthesis. This is indicated by the EDS results obtained from Points 1 and 2 in Figure 3, which both show a high percentage of strontium and sulfur, but a low percentage of carbon and oxygen. However, point 3 in Figure 3 shows a higher percentage of carbon, oxygen, and lower percentage of sulfur, indicating that some progress towards the formation of strontium carbonate has been made in this area. Overall, these results suggest that a longer mechanochemical synthesis time is required to achieve complete conversion of sulfated celestite to strontium carbonate.

Based on the EDS analysis results shown in Figure 4, it can be observed that the percentage of S element (% wt.) in the strontium carbonate (SrCO_3) compound produced through a 1:1.0 stoichiometric ratio of $\text{SrSO}_4:(\text{NH}_4)_2\text{CO}_3$ and 200 min of mechanochemical synthesis is significantly lower compared to the results obtained from the 10-minute synthesis process. The EDS analysis indicates that the S percentage (% wt.) for point 1, 2, and 3 points are 0.15%, 0.18%, and 0.25%, respectively. These values are considerably lower than the S percentage (% wt.) obtained for points 1, 2, and 3 in the 10-minute synthesis process, which were 15.20%, 16.13%, and 4.05%, respectively. This suggests that the sulfate compound in the original structure has been successfully converted into a carbonate compound through the 200-minute mechanochemical synthesis process.

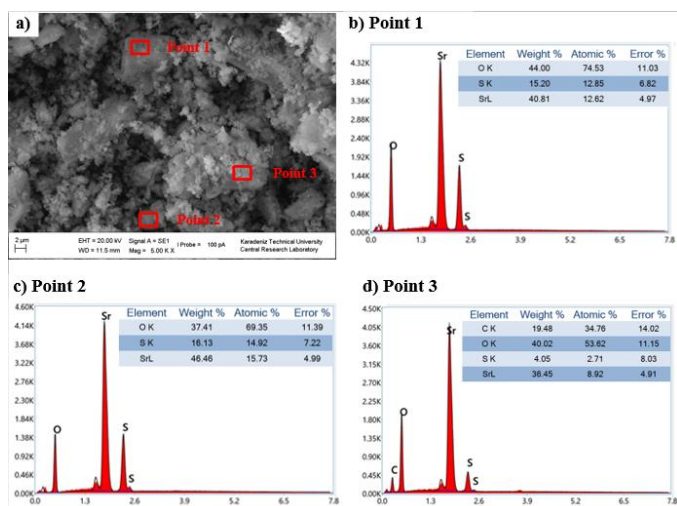


Figure 3. EDS results of powders subjected to 10 minute mechanochemical synthesis.

In summary, the analysis and interpretation of the SEM and EDS results indicate that a longer duration of mechanochemical synthesis is necessary to achieve complete conversion of sulfated celestite to strontium carbonate. The decrease in sulfur content in the strontium carbonate compound produced after 200 minutes of synthesis confirms successful conversion and supports the efficacy of the extended synthesis time in promoting the desired chemical transformation. Based on the SEM images and EDS analysis, it is evident that a 10-minute synthesis duration is not sufficient to achieve complete conversion of sulfated celestite to strontium carbonate. This suggests that an extended synthesis duration leads to a more complete conversion of SrSO_4 to SrCO_3 . The EDS analysis in Figure 4 further supports this observation, as the sulfur content (% wt.) decreases significantly in the strontium carbonate samples synthesized for 100 and 200 minutes compared to the 10-minute synthesis process. This confirms that the sulfate compound in the original structure is successfully transformed into the carbonate compound through the longer mechanochemical synthesis durations.

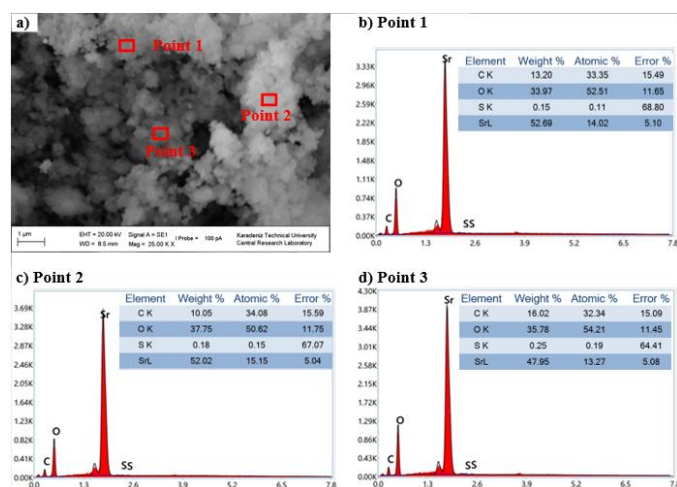


Figure 4. EDS results of powders subjected to 200 minute mechanochemical synthesis.

Particles ranging in size from approximately $10\ \mu\text{m}$ to $100\ \mu\text{m}$ were obtained after a 10-minute synthesis process. These particles exhibited sharp and irregular shapes, indicating the presence of SrCO_3 on their outer shells and the occurrence of breakage during the process. According to the particle size distribution, the average particle size decreased to $6.721\ \mu\text{m}$ after a 10-minute mechanochemical synthesis. This suggests a reduction in particle size compared to the initial sample. Strontium carbonate particles produced through mechanochemical synthesis for 100 minutes exhibited an average particle size of $4.257\ \mu\text{m}$. This indicates further reduction in particle size compared to the 10-minute synthesis. The strontium carbonate particles obtained after 200 minutes of mechanochemical synthesis. The prolonged synthesis duration resulted in a significant decrease in particle size, making it challenging to identify individual particle shapes. Overall, the results indicate that increasing the duration of mechanochemical synthesis led to a decrease in the particle size of the strontium carbonate particles. The particles became smaller and exhibited a more homogeneous size distribution with longer synthesis durations.

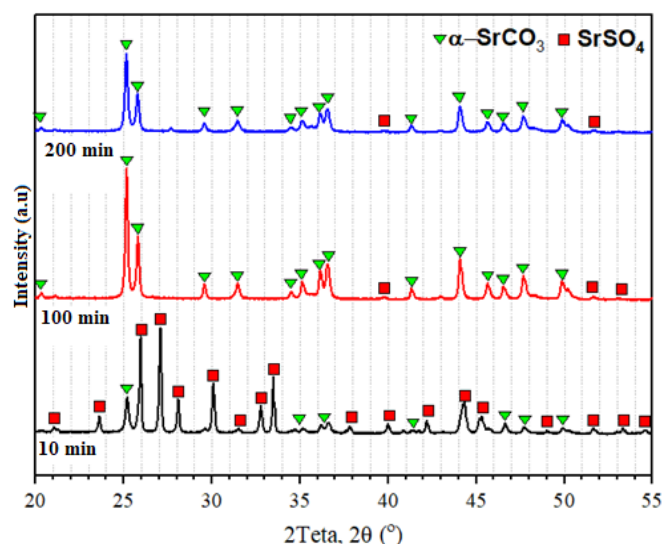


Figure 5. The X-ray diffraction patterns obtained after mechanochemical synthesis with different times.

Figure 5 displays the X-ray diffraction patterns obtained at different synthesis times (10 min, 100 min, and 200 min) for a 1:1.0 stoichiometric ratio of $\text{SrSO}_4:(\text{NH}_4)_2\text{CO}_3$ using mechanochemical synthesis. At 10 minutes of synthesis, the pattern showed peaks for both SrSO_4 and SrCO_3 . However, increasing the synthesis time to 100 minutes led to approximately 86% of the celestite ore converting into SrCO_3 (determined by Rietveld refinement analysis), and this percentage increased to 92% after 200 minutes of synthesis. The X-ray diffraction patterns revealed that the SrCO_3 peaks increased at 100 minutes of synthesis but decreased at 200 minutes, suggesting that extended synthesis times beyond a certain point cause structural distortions and a decrease in crystal size for SrCO_3 . This variation in X-ray diffraction patterns due to synthesis time was observed for other stoichiometric ratios as well.

DTA and TGA analyses were performed to determine the thermal decomposition temperatures of SrCO_3 in transformation processes carried out at synthesis durations. DTA and TGA analyses applied to SrCO_3 compounds produced by

mechanochemical transformation performed at 1:1.0 stoichiometric ratio of $\text{SrSO}_4:(\text{NH}_4)_2\text{CO}_3$ and for 10, 100, and 200 minutes are presented in Figure 6 and Figure 7, respectively. Two different endothermic peaks were observed in the DTA graph showing the phase transformation and thermal decomposition of SrCO_3 for each synthesis duration at 1:1.0 stoichiometric ratio (Figure 6). No transformation peaks related to different compositions were detected outside these endothermic peaks. The transformation temperatures in DTA curves for different synthesis durations were found to decrease with increasing synthesis duration. The temperature at which strontium carbonate begins to thermally decompose was determined as 1000°C for the shortest synthesis duration, while this temperature decreased to 885°C and then to 800°C as the synthesis duration increased. The increase in the energy of the particles in the mechanochemical synthesis process (due to the decrease in particle size) with the synthesis duration causes the thermal decomposition temperature of strontium carbonate to change. The lower intensity of endothermic peak number 2, which was the main focus for the 10-minute synthesis duration, compared to the other synthesis durations (100 and 200 minutes) indicates a lower amount of SrCO_3 formation. This confirms the findings from SEM and XRD analyses. When the TGA curve for different synthesis durations was examined for the fixed stoichiometry of 1:1.0 (Figure 7), the lowest weight loss (%6.5) was observed again for the 10-minute synthesis duration, which confirms the DTA data. The conversion rate of the sulfate compound in celestite to strontium carbonate and the weight loss in the same proportion increase with the increase in mechanochemical synthesis duration. The instant total weight loss at 1200°C for the maximum synthesis duration of 200 minutes is approximately 15.1%. One study, which is related to the celestite ore, results revealed a significant decrease in the reaction temperature as the milling time increased. Specifically, after 1 minute of disc milling, the reaction temperature decreased from 973°C to 892°C . Similarly, with 45 minutes of planetary ball milling, a reduction in the reaction temperature was observed. This finding suggests that longer milling durations promote more efficient carbothermic reduction, leading to a lower required reaction temperature [17].

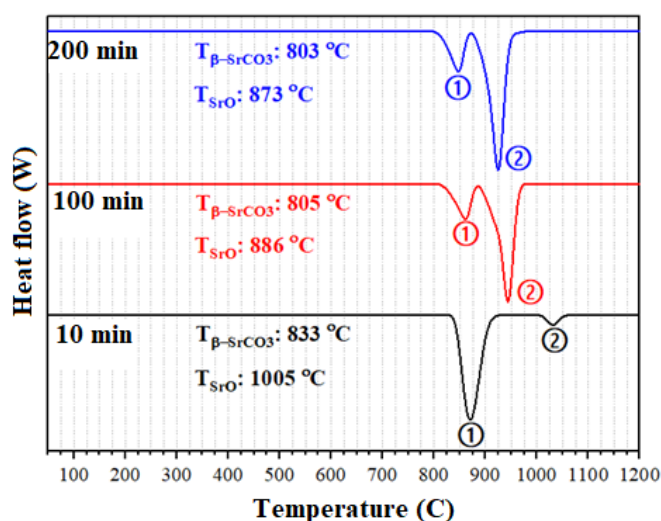


Figure 6. DTA curves obtained after the mechanochemical synthesis process at different times.

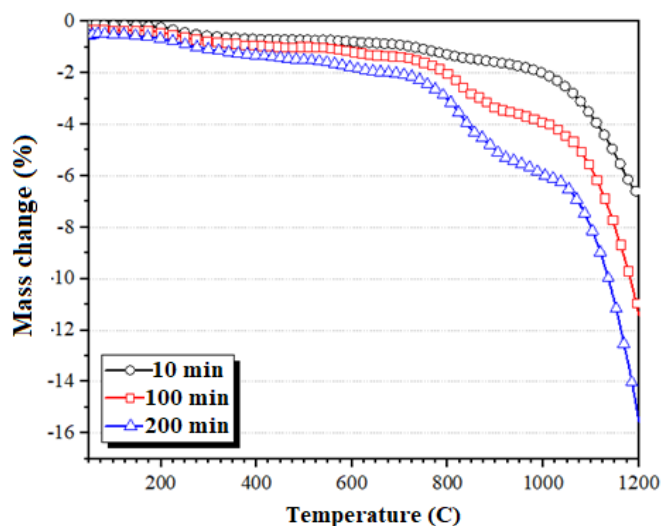


Figure 7. TGA curves obtained after the mechanochemical synthesis process at different times.

Mechanochemical synthesis is a promising method for the production of advanced materials due to its low cost, high efficiency, and environmentally friendly nature. In this process, the reactants are subjected to mechanical force and deformation, leading to solid-state reactions that result in the formation of new materials. However, the reaction temperature and time are important factors that can affect the outcome of the reaction. In this discussion, we will focus on the mechanism behind the decrease in reaction temperature with an increase in mechanochemical synthesis time.

First, it is important to understand the concept of milling energy, which refers to the amount of energy imparted to the reactants during the milling process. The milling energy can affect the reaction kinetics and the thermodynamics of the system. In the case of mechanochemical synthesis, the milling energy can cause deformation and defects in the crystal structure of the reactants, leading to an increase in the reactivity of the system.

The decrease in reaction temperature with an increase in mechanochemical synthesis time can be attributed to several factors. One of the main factors is the increase in surface area of the reactants as a result of the milling process. The increased surface area leads to a higher concentration of reactive sites, which can promote the reaction at lower temperatures [18, 19]. Another factor is the formation of defects and dislocations in the crystal structure of the reactants during the milling process. These defects can serve as nucleation sites for the reaction, reducing the activation energy required for the reaction to occur [20]. Additionally, the deformation of the crystal structure can lead to the formation of non-equilibrium phases, which may have lower reaction temperatures compared to the equilibrium phases. Furthermore, the increase in milling time can lead to the formation of reactive intermediates, such as metastable phases, that can promote the reaction at lower temperatures. These intermediates may have different chemical and physical properties compared to the starting materials and can act as catalysts for the reaction. Finally, the increase in milling time can lead to the formation of amorphous phases, which have higher reactivity compared to crystalline phases. The amorphous phases have a disordered atomic structure, which can provide more reactive sites for the reaction to occur. The amorphous phases can also have a lower activation energy for the reaction,

leading to a decrease in the reaction temperature. In summary, the decrease in reaction temperature with an increase in mechanochemical synthesis time can be attributed to several factors, including the increase in surface area, the formation of defects and dislocations, the formation of reactive intermediates, and the formation of amorphous phases. These factors can all contribute to the increased reactivity of the system, leading to a decrease in the activation energy and the reaction temperature. Understanding these mechanisms is important for the design and optimization of mechanochemical synthesis processes for the production of advanced materials.

4. Conclusions

The main objective of this study was to investigate how mechanochemical synthesis time affects the decomposition of sulfated celestite ore and the formation of strontium carbonate, using various characterization techniques. The results indicate that after 100 minutes of synthesis time, approximately 86.1% of celestite ore is transformed to SrCO_3 , which increases to 92.2% after 200 minutes of synthesis time. The intensity of SrCO_3 peaks also increases at 100 minutes of synthesis time but decreases at 200 minutes, suggesting a disruption in the crystal structure and a reduction in crystal size. The transformation temperatures in DTA curves decrease with increasing synthesis duration due to the increase in energy of particles during the mechanochemical synthesis process. Additionally, the conversion rate of sulfate compound in celestite to strontium carbonate and the weight loss in the same proportion increase with an increase in mechanochemical synthesis duration. These findings provide valuable insights into the mechanistic aspects of strontium carbonate decomposition.

Acknowledgments

This research paper was supported by the TUBİTAK-ARDEB with 119M111 project number. Karadeniz Technical University Department of Scientific Research Project also supported FDK-2018-7685 and FBA-2019-8162 project numbers.

Author contributions

Kürşat İcin: Conceptualization; Data curation; Formal analysis; Sümran Bilgin: Funding acquisition, Investigation; Sefa Emre Sünbül: Methodology; Sultan Öztürk Project administration, Resources, Supervision.

References

- İcin, K., Öztürk, S., Çakıl, D. D., Sünbül, S. E., Ergin, İ., Özçelik, B., Investigation of nano-crystalline strontium hexaferrite magnet powder from mill scale waste by the mechanochemical synthesis: Effect of the annealing temperature. *Materials Chemistry and Physics* **2022**, 290, 126513
- Yan, F., Zhang, X., Asselin, E., Duan, D., Li, Z., Preparation of strontium carbonate via celestite leaching in NaHCO_3 using two interconnected reactors. *Hydrometallurgy* **2021**, 204, 105729
- Liu, X., Li, Y., Zeng, L., Li, X., Chen, N., Bai, S., He, H., Wang, Q., Zhang, C., A Review on Energy Mechanochemistry: Approaching Advanced Energy Materials with Greener Force. **2022**, 34 (46):2108327
- Ardila-Fierro, K. J., Hernández, J. G., Sustainability Assessment of Mechanochemistry by Using the Twelve Principles of Green Chemistry. **2021**, 14 (10):2145-2162
- Dayani, N., AmirArjmand, A., Nouri-Khezrabad, M., Hasani, S., High-efficiency mechanochemical synthesis of Strontium carbonate nanopowder from Celestite. **2021**, 18 (1):24-31
- El-Sadek, M. H., Farahat, M. M., Ali, H. H., Zaki, Z. I., Synthesis of SrTiO_3 from celestite and rutile by mechanical activation assisted Solid-State reaction. *Advanced Powder Technology* **2022**, 33 (5):103548
- Erdemoğlu, M., Aydoğan, S., Canbazoglu, M., A kinetic study on the conversion of celestite (SrSO_4) to SrCO_3 by mechanochemical processing. *Hydrometallurgy* **2007**, 86 (1):1-5
- Obut, A., Baláz, P., Girgin, İ., Direct mechanochemical conversion of celestite to SrCO_3 . *Minerals Engineering* **2006**, 19 (11):1185-1190
- Bingöl, D., Aydoğan, S., Bozbaş, S. K., Production of SrCO_3 and $(\text{NH}_4)_2\text{SO}_4$ by the dry mechanochemical processing of celestite. *Journal of Industrial and Engineering Chemistry* **2012**, 18 (2):834-838
- Bowmaker, G. A., Solvent-assisted mechanochemistry. *Chemical Communications* **2013**, 49 (4):334-348
- Martín-Perales, A. I., Balu, A. M., Malpartida, I., Luque, R., Prospects for the combination of mechanochemistry and flow applied to catalytic transformations. *Current Opinion in Green and Sustainable Chemistry* **2022**, 38, 100714
- Takacs, L., The historical development of mechanochemistry. *Chemical Society Reviews* **2013**, 42 (18):7649-7659
- Black, A. L., Lenhardt, J. M., Craig, S. L., From molecular mechanochemistry to stress-responsive materials. *Journal of Materials Chemistry* **2011**, 21 (6):1655-1663
- Tole, I., Habermehl-Cwirzen, K., Rajczakowska, M., Cwirzen, A. Activation of a Raw Clay by Mechanochemical Process—Effects of Various Parameters on the Process Efficiency and Cementitious Properties Materials [Online], **2018**
- Bingöl, D., Aydoğan, S., Bozbaş, S. K., Optimization of the Wet Mechanochemical Process Conditions of SrSO_4 to SrCO_3 and $(\text{NH}_4)_2\text{SO}_4$ by Using Response Surface Methodology. *Metallurgical and Materials Transactions B* **2012**, 43 (5):1214-1219
- Tiwary, R. K., Narayan, S. P., Pandey, O. P., Preparation of strontium hexaferrite magnets from celestite and iron ore fines by mechanochemical route. *Mineral Processing and Extractive Metallurgy* **2009**, 118 (4):201-204
- Sezer, R., Hızlı, İ. G., Bilen, A., Ertürk, S., Arslan, C. J. M. B., Effect of Mechanical Activation on Roasting of Celestite Ore. **2017**, (11):53-59
- Tan, Q., Li, J., Recycling Metals from Wastes: A Novel Application of Mechanochemistry. *Environmental Science & Technology* **2015**, 49 (10):5849-5861
- Tsuzuki, T., McCormick, P. G., ZnO nanoparticles synthesised by mechanochemical processing. *Scripta Materialia* **2001**, 44 (8-9):1731-1734
- Wang, R., Zhu, Z., Tan, S., Guo, J., Xu, Z., Mechanochemical degradation of brominated flame retardants in waste printed circuit boards by Ball Milling. *Journal of hazardous materials* **2020**, 385, 121509